TITLE:

Tricuspid valve leaflet remodeling in sheep with biventricular heart failure: A comparison between leaflets

AUTHORS:

Colton J. Kostelnik[a,†], William D. Meador[a,†], Chien-Yu Lin[a], Mrudang Mathur[b], Marcin Malinowski[c,d], Tomasz Jazwiec[c,e], Zuzanna Malinowska[g], Magda L. Piekarska[c,d], Boguslaw Gaweda[c,f], Tomasz A. Timek[c], Manuel K. Rausch[a,b,g,*]

AFFILITATIONS:

[a]Department of Biomedical Engineering, The University of Texas at Austin, Austin, TX, USA

[b]Department of Mechanical Engineering, The University of Texas at Austin, Austin, TX, USA

[c]Division of Cardiothoracic Surgery, Corewell Health, Grand Rapids, MI, USA

[d]Department of Cardiac Surgery, Medical University of Silesia, School of Medicine in Katowice, Katowice, Poland

[e]Department of Cardiac, Vascular, and Endovascular Surgery and Transplantology, Medical University of Silesia in Katowice, Silesian Centre for Heart Disease, Zabrze, Poland

[f]Department of Cardiac Surgery, Clinical District Hospital No. 2, Faculty of Medicine University of Rzeszow, Rzeszow, Poland

[g]Department of Aerospace Engineering & Engineering Mechanics, The University of Texas at Austin, Austin, TX, USA

* Corresponding Author: Manuel K. Rausch, manuel.rausch@utexas.edu, +1 (512) 471-5147, 2501 Speedway, EER Building, Room 7.620

† Colton Kostelnik and William Meador are co-first authors

ABSTRACT: Tricuspid valve leaflets are dynamic tissues that can respond to altered biomechanical and hemodynamic loads. Each leaflet has unique structural and mechanical properties, leading to differential *in vivo* strains. We hypothesized that these intrinsic differences drive heterogeneous, disease-induced remodeling between the leaflets. Although we previously reported significant remodeling changes in the anterior leaflet, the responses among the other two leaflets have not been reported. Using a sheep model of biventricular heart failure, we compared the remodeling responses between all tricuspid leaflets. Our results show that the anterior leaflet underwent the most significant remodeling, while the septal and posterior leaflets exhibited similar but less pronounced changes. We found several between-leaflet differences in key structural and mechanical metrics that have been shown to contribute to valvular dysfunction. These findings underscore the need to consider leaflet-specific remodeling to fully understand tricuspid valve dysfunction and to develop targeted therapies for its treatment and more accurate computational models.

KEYWORDS: Leaflet-specific Remodeling; Tachycardia-induced Cardiomyopathy; Biaxial Testing; Histology; Two-photon Microscopy

STATEMENT OF SIGNIFICANCE:

Our study is significant as it advances our understanding of tricuspid valve remodeling by providing a comprehensive analysis of all three leaflets in a sheep model of biventricular heart failure. Unlike prior works that focused primarily on the anterior leaflet or generalized leaflet changes, we integrated morphological, histological, immunohistochemistry, biaxial mechanical testing, and two-photon microscopy to quantify differences between all three tricuspid valve leaflets (anterior, posterior, and septal) across multiple functional scales. This comprehensive approach highlights the unique remodeling response of each leaflet. Our findings offer critical insights for developing targeted therapeutic strategies and improving computational models of disease progression.

GRAPHICAL ABSTRACT

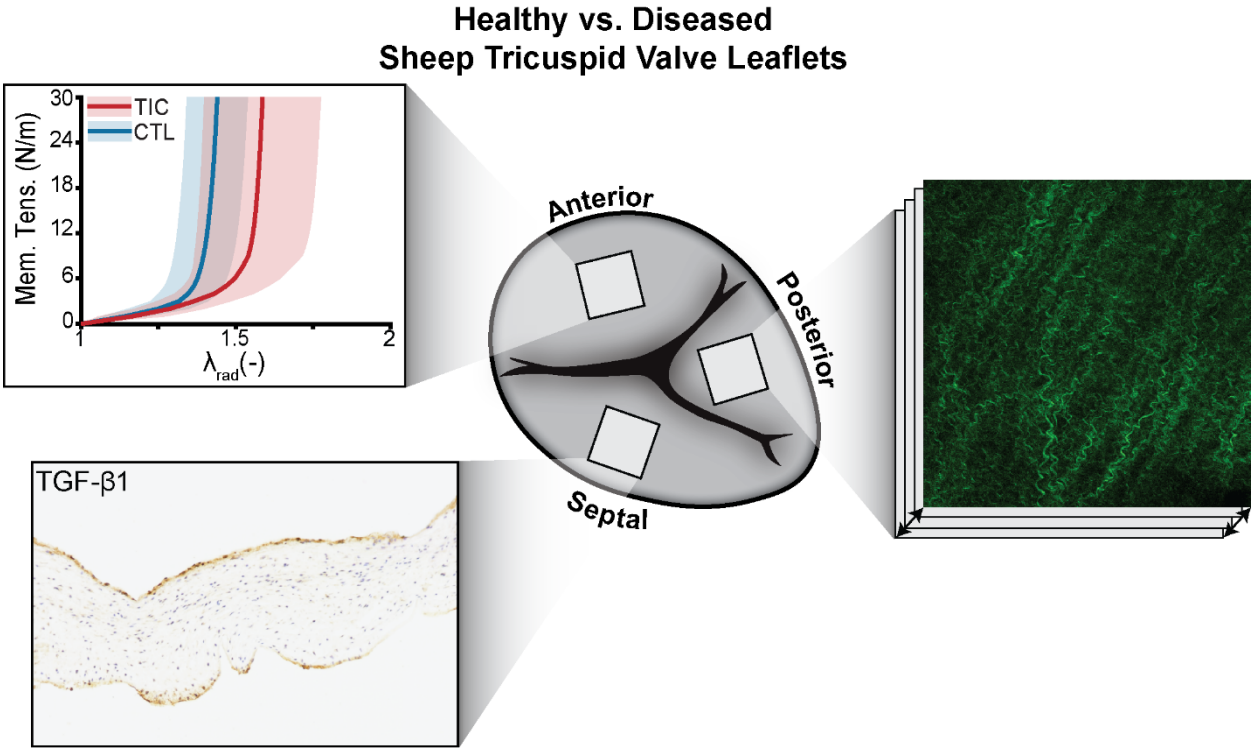

1. INTRODUCTION

Tricuspid regurgitation (TR) is a highly prevalent echocardiographic finding detected in 82-86% of people [1]. Approximately 1.6 million Americans suffer from moderate to severe TR, which, if left untreated, can lead to multiple cardiovascular complications [2]. More than 90% of patients with severe TR exhibit a "functional" etiology, wherein the valve dysfunction is secondary to other cardiac pathologies such as left-sided heart disease or pulmonary hypertension [3–5]. The valve itself has historically been considered structurally and mechanically intact, and this assumption has guided a conservative treatment approach that focuses on managing the primary condition to resolve any TR [6,7]. However, early surgical repair of the tricuspid valve during mitral or aortic valve surgeries has shown promise in improving patient outcomes and diminishing cardiac-related mortality [8,9]. Despite this evolution of TR management, it remains undertreated and poorly understood.

Heart valve leaflets were once considered "passive flaps" that merely coordinated unidirectional blood flow between the heart chambers akin to a check valve. However, we now know that heart valve leaflets are highly organized tissues with multiple cell types and intricate extracellular architectures that actively remodel by contracting and reshaping to optimize coaptation [10–12]. In diseased patients, leaflet remodeling induces a fibrotic response (i.e., maladapt), which impedes proper kinematics and coaptation [13]. Animal studies of heart failure and chronic ischemia have shown that maladaptive changes in the mitral valve leaflets manifest by increased size, thickness, and stiffness [13–16]. We have demonstrated in two animal models that similar remodeling patterns exist in the tricuspid valve leaflets (e.g., increases in area, thickness, and stiffness) in response to altered biomechanical and

81 hemodynamic loads [17,18]. These remodeling-induced leaflet changes affect leaflet stresses
82 and leaflet contact area (i.e., coaptation area), indicating that valve function is sensitive to
83 leaflet maladaptation [19].

84 Moreover, we have previously demonstrated that the tricuspid leaflets in healthy sheep
85 exhibit distinct, leaflet-specific properties, including unique morphology, mechanical properties,
86 and *in vivo* mechanics [20,21]. In our prior study of tricuspid valve maladaptation, we found
87 that the anterior tricuspid leaflet exhibited significant remodeling changes on all functional
88 scales in sheep with biventricular heart failure after 2-3 weeks of tachycardia-induced
89 cardiomyopathy (TIC) [17]. Building on this work, here we aim to quantify the remodeling
90 changes in the septal and posterior tricuspid leaflets from the same sheep and compare the
91 remodeling patterns across all three leaflets. We hypothesize that the leaflet-specific
92 mechanics drive heterogeneous remodeling responses between the tricuspid leaflets.
93 Specifically, we hypothesize that the TIC anterior leaflets exhibit the most significant
94 remodeling changes relative to its control due to its larger *in vivo* area strains, while the TIC
95 septal and posterior leaflets remodel to a lesser extent [20]. This distinction of differential
96 remodeling may be vital in uncovering potential therapeutic targets tailored to specific leaflets
97 and informing computational models of disease progression.

98 **2. MATERIALS & METHODS**

99 **2.1 Animal Model, Medication, and Procedures**

100 This research complied in accordance with the Principles of Laboratory Animal Care,
101 formulated by the National Society for Medical Research, and adhered to protocols outlined in
102 the Guide for Care and Use of Laboratory Animals, published by the National Institutes of

103 Health. Additionally, this protocol was developed, reviewed and performed in accordance with
104 the approval of a local Institutional Animal Care and Use Committee at Corewell Health. The
105 specific approval numbers are 2017-357, 2018-402, 2018427, and 2018-439.

106 The TIC sheep model used in this study has been previously described in detail and
107 demonstrated as a reliable and repeatable model of biventricular heart failure in sheep [22].
108 Detailed descriptions of the animal model, medications, and procedures are available in our
109 prior work [17]. We randomly assigned adult male Dorsett sheep to either the control (CTL) (n =
110 17, 59.9 ± 4.6 kg) or TIC (n = 33, 60.1 ± 5.3 kg) groups. Before initiating pacing, we monitored
111 baseline ventricular function and valvular competence in all animals using epicardial
112 echocardiography. The TIC sheep were then subject to a 180-260 beats per minute pacing
113 protocol for 19 ± 6 days. Following the pacing period, we performed the terminal procedure on
114 all TIC sheep and recorded hemodynamic and echocardiographic data over three cardiac cycles.
115 In CTL sheep, we performed the terminal procedure following baseline epicardial
116 echocardiography. We reported all hemodynamic and echocardiographic data in Table 1 of our
117 previous study [17]. After completing the terminal procedures, we isolated the tricuspid valve
118 from each animal for further analysis.

119 For disclosure, we previously published data on the anterior leaflet morphology,
120 thickness, biaxial mechanics, histology, collagen content, and two-photon microscopy from the
121 sheep included in this study [17]. We include these data here again with expressed permission
122 from the editorial office.

123 **2.2 Morphology and Storage**

124 We isolated the tricuspid valve leaflet complex from each heart and separated the
125 leaflets at the posterior-septal commissure. We then floated each valve on 1x PBS and imaged
126 them on a calibrated grid to compare morphological measures such as leaflet area between CTL
127 and TIC animals (Figure 1a). The leaflets were then separated and cryopreserved in DMEM
128 (VWR L0101-0500, Radnor, PA, USA) containing 10% DMSO (VWR BDH1115-1LP) supplemented
129 with a protease inhibitor (ThermoFisher, A32953, Weltham, MA, USA) and stored at -80°C until
130 tested. Cryogenic studies have shown that the mechanical properties of soft tissues were
131 minimally impacted after storage at temperatures below 0°C [23,24].

132 **2.3 Histology and Immunohistochemistry**

133 After thawing, we cut and fixed radial strips (from near-annulus to free edge) of all
134 leaflets in 10% neutral buffered formalin for 24 hours and then transferred to 70% ethanol for
135 long-term storage. The fixed leaflet strips were shipped to a histological service (HistoServ Inc.,
136 Amaranth, MD) for embedding, sectioning at 5 μm slice thickness, and staining with
137 Hematoxylin & Eosin and immunohistochemistry. Using a light microscope (Ti2-E High-content
138 Analysis System, Nikon, Tokyo, Japan) with a 10x objective, we acquired full section images for
139 all histological and immunohistochemistry sections. After imaging, we used ImageJ (National
140 Institutes of Health, Bethesda, MD, USA) to measure the total length of the tissue section along
141 the atrial surface and separated each section into three equidistant regions (i.e., near-annulus,
142 belly, and free edge). We then measured the normal vectors between the atrial and ventricular
143 surfaces at three random positions within each region. Finally, we averaged all regional
144 thickness measurements into the total leaflet thickness for each sample.

145 We assessed four cellular markers associated with remodeling processes: (i) alpha-
146 smooth muscle actin (α-SMA) (Abcam, ab5694, 1:600, Cambridge, MA, US), (ii) Ki67 (Abcam,
147 ab15580, 1:1250, Cambridge, MA, US), (iii) matrix-metalloprotease 13 (MMP13) (Abcam,
148 ab39012, 1:50, Cambridge, MA, US), and (iv) transforming growth factor beta-1 (TGF-β1)
149 (Abcam, ab9758, 1:100, Cambridge, MA, US). A custom MATLAB program segmented the full
150 cross-sectional leaflet image into three equidistant length regions (near-annulus, belly, and free
151 edge). We then interpolated ten thickness regions of the leaflet cross-sectional images between
152 the atrial and ventricular surfaces, resulting in a total of 30 regions. Each region underwent
153 analysis through our validated custom MATLAB program to spatially resolve the presence of
154 positive pixels and normalize their percentage to the total pixels in that region [17].

155 **2.4 Biaxial testing**

156 We tested leaflet samples and analyzed the biaxial mechanics using the methods fully
157 described in our prior work [17,21]. First, we isolated a 7x7 mm square sample from the belly
158 region of each septal, anterior, and posterior leaflet. We then applied four fiducial markers to
159 the atrial surface of each sample to enable strain tracking during testing. Before testing, we
160 measured sample thickness at four locations using a digital thickness gauge (547-500S,
161 Mitutoyo Corp., Kawasaki, Japan) and captured an image of the stress-free configuration on a
162 calibrated grid. Next, we mounted all samples on a biaxial testing device (Biotester, CellScale,
163 Waterloo, ON, Canada) submerged in 37°C 1x PBS, and performed ten preconditioning cycles of
164 equibiaxial extension to 300 mN followed by two final equibiaxial cycles to 300 mN. While
165 testing, we continuously captured circumferential and radial forces and images of the fiducial
166 markers at 5 Hz.

167 We used the image analysis software Labjoy (CellScale, Waterloo, ON, Canada) to track
168 the coordinates of the fiducial markers throughout testing. Our analysis focused on the
169 downstroke of the last loading cycle, and we reported membrane tension-stretch data relative
170 to the preloaded stress-free configuration. To characterize tissue deformation, we computed
171 the deformation gradient tensor $\boldsymbol{F}$ relative to the stress-free reference state and derived the
172 right Cauchy-Green deformation tensor $\boldsymbol{C} = \boldsymbol{F}^T\boldsymbol{F}$ to determine in-plane stretches throughout
173 the experiment. Membrane tension was calculated by dividing the measured force by the
174 perpendicular rake-to-rake distance in the deformed configuration at each time point.

175 To quantitatively compare the nonlinear membrane tension-stretch curves between CTL
176 and TIC for all three leaflets, we analyzed four characteristic metrics of the resulting nonlinear J-
177 shaped curves: (1) toe stiffness, defined as the slope in the lower linear region of the curve; (2)
178 calf stiffness, measured as the slope near 20 N/m membrane tension; (3) transition stretch,
179 identified as the stretch value at the curve's inflection point (approximated by the intersection
180 of toe and calf stiffness lines); and (4) anisotropy index, calculated as the ratio of
181 circumferential to radial stretches at 20 N/m tension.

182 **2.5 Two-Photon Microscopy**

183 We imaged and analyzed the collagen microstructure and cell nuclei using the same
184 two-photon microscopy methods described in our previous work [21,25]. The mechanically
185 tested square sample from the leaflet belly was briefly stained with Hoechst 33342 (Thermo
186 Fischer Scientific, Hoechst 33342, Waltham, MA, US) for 20 minutes to visualize the cell nuclei.
187 The tissue sample was then optically cleared under sonication for 30 minutes in a solution
188 containing glycerol:DMSO: 5x PBS at 50:30:20% (v/v), respectively [26]. Next, we imaged the

189 leaflet samples with a two-photon microscope (Ultima IV, Bruker, Billerica, MA, USA) to
190 visualize collagen fiber orientation via second harmonic generation (SHG) and cell nuclei via
191 fluorescent excitation, respectively. Before imaging, the leaflet samples were placed on a foil-
192 lined glass slide with a coverslip to flatten the sample during imaging without imposing any
193 stresses. We captured images from the atrial to the ventricular surface at three centrally
194 located regions (500x500 μm, for each region) using a 20x water-immersion objective
195 (Olympus, XLUMPLFLN, Center Valley, PA, US) at an excitation wavelength of 900 nm for SHG
196 and 800 nm for fluorescence. We collected the backscattered SHG signal through a PMT
197 channel filter (460 nm ± 25 nm) and acquired a z-stack of images at a step size of 10 μm. To
198 analyze the SHG images, we used the orientation distribution analysis with the Gaussian
199 gradient method in the ImageJ plugin OrientationJ (National Institutes of Health, Bethesda, MD,
200 USA). We then averaged and interpolated across the three z-stacks for each leaflet sample and
201 then fit a symmetric von Mises distribution to each histogram to estimate the mean fiber angle
202 μ and the fiber orientation concentration κ [27]. To analyze the cell nuclei morphology and
203 orientation, we used our custom-validated MATLAB code to quantify individual nuclei contours,
204 nuclear aspect ratio (NAR), and circularity from each image [17]. Similarly, we fit von Mises
205 distributions to the nuclear orientation histograms and normal distributions to the NAR and
206 circularity histograms.

207 **2.6 Statistical Analysis**

208 For all morphological, thickness, biaxial, and two-photon distribution data comparisons,
209 we used a linear mixed effects model in R via the package *afex* (Version 4.4.2). Our models
210 included fixed effects for animal group (CTL vs. TIC), leaflet type (anterior, posterior, septal),

direction (X vs. Y) where applicable, and their interactions. Random intercepts were included for subjects to account for repeated measurements within individuals. We performed a Type III ANOVA analysis with Satterthwaite's method to assess the significance of main effects and interactions. We then performed one-tailed pairwise comparisons between CTL and TIC animals for each leaflet type using the *emmeans* package in R, and performed two-tailed pairwise comparisons using Tukey's method to compare between leaflets from the CTL and TIC animals. We defined statistical significance as p-values less than 0.05. We reported data as mean with the standard deviation of the mean.

3. RESULTS

3.1 Animal model outcomes

We isolated 17 tricuspid valves from CTL sheep and 33 tricuspid valves from TIC sheep. Our study included all tricuspid valve leaflets to assess their geometric and functional changes. Echocardiographic and hemodynamic evaluations revealed significant parameter changes in TIC sheep consistent with biventricular dysfunction and functional TR. Key findings included reduced biventricular ejection fraction, evidence of biventricular remodeling, tricuspid valve annular dilation, and increased severity of TR (Table 1) [17].

3.2 TIC-induced changes to leaflet geometry

Leaflet geometry, including area and thickness, is critical for assessing valve function in TR [16]. While prior studies detailed size and shape differences in healthy tricuspid valve leaflets [21], geometric changes in TIC leaflets remain underexplored. Building on our previous findings of geometric changes in TIC anterior leaflets [17], we hypothesized that all TIC leaflets

232 would exhibit distinct geometric changes. To test this, we quantified leaflet area and thickness
233 across all leaflets (Figure 1a, Figures 2a–c).

234 We compared the leaflet area measurements between CTL and TIC animals, and we
235 found that TIC septal and anterior leaflets significantly increased in area compared to
236 respective CTL leaflets ($p = 0.009$ and $p = 0.002$, respectively) (Figure 1b-c). In contrast, the TIC
237 posterior leaflets' area remained unchanged ($p = 0.153$) (Figure 1d). We found a significant
238 interaction between animal group and leaflet type ($p = 0.044$), highlighting the heterogeneous
239 remodeling response among leaflets. For instance, in CTL animals, we found that the septal
240 leaflet area was significantly smaller than the anterior and posterior leaflets (both $p \leq 0.0001$),
241 while among TIC animals, leaflet area differed significantly across all leaflets (all $p \leq 0.0001$). We
242 compared the average thickness between CTL and TIC animals from our histological cross-
243 sectional images, and we found that only the TIC anterior and posterior leaflets significantly
244 increased ($p = 0.024$ and $p = 0.033$, respectively) in thickness compared to their respective CTL
245 leaflets (Figures 2d-f). However, we did not detect any significant differences between the
246 leaflets of CTL animals or between the leaflets of TIC animals. These findings highlight the
247 distinct growth of each tricuspid leaflet under disease conditions, suggesting differential
248 remodeling exists between the tricuspid leaflets.

249 **3.3 TIC-induced changes to leaflet mechanics**

250 Leaflet remodeling in heart failure patients alters the mechanical properties of the valve
251 leaflets [13]. Building on our previous findings of altered anterior tricuspid leaflet mechanics in
252 TIC animals [17], we hypothesized that each TIC leaflet would exhibit distinct and leaflet-
253 specific changes in mechanical behavior. All leaflets exhibited the classic J-shaped loading curve

254 of biological collagenous tissues (Figures 3a, 3d, 3g) [28]. Our analysis did not detect any
255 significant change in calf stiffnesses between CTL and TIC animals for any of the leaflets, in
256 either the circumferential and radial direction (Figures 3b, 3e, 3h). However, we did find that
257 the TIC anterior leaflet exhibited a significant increase in circumferential toe stiffness when
258 compared to CTL ($p = 0.022$). In contrast, we failed to detect a significant change in the
259 posterior and septal leaflets' toe stiffnesses. Our between-leaflet comparison revealed that
260 circumferential toe stiffness differed significantly between the TIC septal and anterior leaflets (p
261 $= 0.044$) (Figures 3b and 3e).

262 The most pronounced between-leaflet differences emerged when comparing the
263 transition stretches and anisotropy indices. We found that the anterior leaflet showed a
264 significant decrease in the circumferential transition stretch between CTL and TIC animals ($p =$
265 0.047), while we failed to detect any significant changes in the posterior and septal leaflets
266 (Figure 4 a-c). Our between-leaflet comparison within CTL animals revealed that the posterior
267 leaflet radial transition stretches significantly differed from the other leaflets (anterior-
268 posterior: $p = 0.0009$; septal-posterior: $p \leq 0.0001$). Among the TIC animals, we found that the
269 septal leaflet's circumferential transition stretch was significantly different from the anterior
270 leaflet ($p = 0.036$), while the posterior leaflet's radial transition stretch was significantly
271 different from the other leaflets (anterior-posterior: $p \leq 0.0001$; septal-posterior: $p = 0.0002$).
272 Our analysis of anisotropy indices revealed a near-significant interaction effect between animal
273 group and leaflet type ($p = 0.052$). We found that the septal leaflet anisotropy index
274 significantly decreased ($p = 0.004$) between CTL and TIC animals to a value below 1, indicating
275 larger stretches in the radial direction (Figure 4d). In contrast, the anterior and posterior

276 leaflets retained stable anisotropic properties (Figures 4e and 4f). Our between-leaflet
277 comparison within CTL animals revealed significant differences between all leaflets (septal-
278 anterior: $p = 0.024$; anterior-posterior: $p = 0.021$; septal-posterior: $p \leq 0.0001$). Among TIC
279 animals, the posterior leaflet's anisotropy differed significantly from both the other leaflets
280 (anterior-posterior: $p = 0.0009$; septal-posterior: $p = 0.0005$), revealing a disease-induced shift
281 in the septal leaflet's radial behavior. Overall, TIC induced the most significant remodeling
282 mechanical changes in the septal leaflet. While the CTL septal leaflet exhibited greater
283 circumferential compliance, the TIC septal leaflet remodeled in a manner that resulted in
284 greater radial compliance, aligning its behavior more closely with the anterior and posterior
285 leaflets. These findings underscore the pronounced remodeling of the septal leaflet under
286 disease conditions, leading to altered anisotropy and compliance patterns.

287 **3.4 Increased expression of cellular remodeling markers in TIC leaflets**

288 Pathological activation of valvular endothelial cells (VECs) and valvular interstitial cells
289 (VICs) promotes extracellular matrix (ECM) remodeling through expression, secretion, and
290 degradation of load-bearing proteins [29]. We hypothesized that each TIC leaflet would exhibit
291 elevated expression of remodeling markers, with variations in the magnitude and region of
292 expression between leaflets. Specifically, we anticipated increased expression of all markers
293 tested (α-SMA, Ki67, MMP13, TGF-β1) [17,18].

294 In the TIC septal leaflets, we observed region-specific increases in all four remodeling
295 markers, particularly in the near-annulus and belly regions, while MMP13 expression decreased
296 at the free edge (Figure 5). These findings align with our previous observations of increased
297 remodeling marker expression in TIC anterior leaflets (Figure 6). In the TIC posterior leaflets,

298 expression of α-SMA and Ki67 increased in the near-annulus region (Figures 7a and 7b). In
299 contrast, the expression levels of MMP13 and TGF-β1 decreased throughout the TIC posterior
300 leaflets (Figures 7c and 7d). Additionally, all TIC leaflets exhibited regionally increased cell nuclei
301 density consistent with elevated Ki67 expression, see Supplementary Figure S1.

302 **3.5 Changes in collagen fiber orientation in TIC leaflets**

303 Collagen fiber orientation is a critical determinant of leaflet stiffness, ensuring
304 mechanical functionality during the cardiac cycle [30]. Building on previous findings of
305 increased fiber dispersion in the TIC anterior leaflets [17], we hypothesized that all TIC leaflets
306 would exhibit increased collagen fiber dispersion. To test this, we fit von Mises probability
307 distribution functions to collagen fiber orientation histograms for leaflets from CTL and TIC
308 animals (Figures 8a, 8c, 8e). We quantified the concentration parameter κ from the collagen
309 fiber orientation histograms and measured fiber dispersion as a function of imaging depth. A
310 large κ value indicates more aligned fibers, while lower values suggest greater dispersion and
311 more isotropic distribution of collagen fibers.

312 Our analysis revealed that the TIC septal and anterior leaflet significantly increased in
313 fiber dispersion near the atrial surface ($p = 0.005$ and $p = 0.011$, respectively) (Figures 8b and
314 8d). In contrast, we failed to detect any significant changes in the fiber dispersion in the other
315 depth regions and throughout the posterior leaflet. Our between-leaflet comparison revealed
316 that a significant difference in fiber dispersion was only present in the TIC animals. We found
317 that the TIC posterior leaflet exhibited significantly different κ values from the other leaflets in
318 the 0-33% depth (D1), nearest the atrial surface (anterior-posterior: $p = 0.017$; septal-posterior:
319 $p = 0.033$). In the 33-67% depth (D2), we found that the TIC septal leaflet was significantly

320 different (p = 0.004) from the anterior leaflet. Additionally, we found that the TIC septal leaflet
321 significantly differed from the other leaflets in the 67-100% depth (D3), nearest the ventricular
322 surface (septal-anterior: p = 0. 0.005; septal-posterior: p = 0.028). Similar analyses revealed cell
323 nuclei of TIC septal leaflets concentrating in the circumferential direction within the 0-33%
324 depth, see Supplementary Fig. 2. In contrast, we observed no notable difference in cell nuclei
325 orientation, nuclear aspect ratio, or circularity between CTL and TIC anterior and posterior
326 leaflets, see Supplementary Fig. 3 and Fig. 4. Overall, we observed that TIC-induced changes
327 resulted in more radially dispersed collagen fibers in TIC septal and anterior leaflets near the
328 atrial surface.

329 **4. DISCUSSION**

330 Our study provides a comprehensive analysis of the heterogeneous remodeling
331 responses of tricuspid valve leaflets in a biventricular heart failure model, highlighting leaflet-
332 specific changes at the tissue and cellular levels. The distinct morphological and mechanical
333 properties between the tricuspid leaflets are essential for maintaining healthy valve function
334 [21,31]. Our findings reveal that biventricular heart failure leads to heterogeneous remodeling
335 between the tricuspid leaflets.

336 At the cellular level, we observed localized profibrotic and degradative responses driving
337 heterogeneous ECM remodeling both between and within tricuspid leaflets [32]. Elevated
338 expression of α-SMA in all TIC leaflets indicates VIC activation as a central mechanism in leaflet
339 remodeling [33,34]. This activation appears localized, with distinctive changes in α-SMA
340 expression within each leaflet, suggesting region-specific remodeling processes. Activated VICs
341 assume a hypersecretory phenotype – known as myofibroblasts – contributing to fibrosis by

342 collagen secretion [33]. The expression of MMP13 is indicative of ECM degradation [17]. In the
343 TIC septal and anterior leaflets' near-annulus and belly regions, elevated expression of these
344 remodeling markers (α-SMA and MMP13) indicate increased matrix turnover. Conversely, the
345 decreased expression of α-SMA and MMP13 in the free edge region of septal and posterior
346 leaflets signify limited ECM turnover. The localization of both Ki67 and TGF-β1 to the
347 endothelial layer TIC leaflets provides evidence of endothelial-to-mesenchymal transition
348 (EndoMT). These findings highlight the critical role of endothelial cells in responding to
349 mechanical stress and regulating fibrotic responses [35]. This regional variation in remodeling
350 markers highlights the leaflet- and region-specific stimuli, possibly related to mechanical
351 loading or biochemical environment, which drive the localized remodeling response [36].
352 Spatially heterogeneous pathological strains imposed by annular dilation or leaflet tethering
353 trigger these responses [37]. Such strains, often localized along the free edge, trigger
354 mechanobiological pathways promoting remodeling within that region of the TIC leaflets
355 [29,38].

356 The tissue and cellular-level changes observed in the tricuspid leaflets after TIC provide
357 mechanistic insights into the functional alterations observed in previous *in vivo* studies of TIC
358 sheep models [39,40]. The TIC septal leaflet exhibited a complex remodeling response
359 characterized by significant geometric, mechanical, and microstructural changes. We observed
360 an increase in leaflet area and a shift in the anisotropy index towards greater radial compliance.
361 This was accompanied by increased collagen fiber dispersion near the atrial surface and
362 elevated expression of α-SMA and MMP13 in the near-annulus and belly regions. These
363 findings collectively indicate enhanced matrix turnover and suggest a compensatory

364 mechanism to accommodate the increased septal-lateral annular dilation observed in TIC
365 animals [32]. The pronounced remodeling observed in the TIC anterior leaflet aligns with
366 previous findings of increased strain in this leaflet during *in vivo* studies [39]. We observed a
367 substantial increase in leaflet area and thickness, accompanied by increased circumferential toe
368 stiffness and decreased circumferential transition stretch. These changes indicate a tissue and
369 cellular-level response to maintain coaptation and valve function in the face of increased area
370 strain and annular dilation associated with TIC [17,39]. In contrast, the posterior leaflet
371 displayed a more stable mechanical profile, with no significant changes in stiffness or transition
372 stretch. However, localized increases in α-SMA and Ki67 expression suggest that while the
373 posterior leaflet may not undergo extensive structural remodeling, it remains responsive to
374 pathological stimuli.

375 The heterogeneous remodeling response observed in our biventricular heart failure
376 model reflects the unique properties of each tricuspid leaflet and the differential mechanical
377 stimuli they experience [20,21]. The TIC model induces complex changes across the tricuspid
378 valve apparatus, including right ventricular remodeling, asymmetric annular dilation, and
379 altered chordal tethering forces [22,39,40]. These extrinsic factors create a diverse mechanical
380 environment, subjecting each leaflet to unique biomechanical stimuli and influencing their
381 individual propensity to remodel.

382 Incorporating these findings into future computational models can significantly enhance
383 our understanding of valvular disease progression, potentially leading to more clinically
384 relevant results. Computational models, informed by the differential remodeling responses
385 observed in the tricuspid valve leaflets, may help simulate various disease scenarios and predict

386 the impact of different therapeutic interventions [19,41]. This approach may allow for a better
387 understanding of the underlying mechanisms driving leaflet-specific remodeling and aid in
388 developing more precise and effective treatment strategies.

389 While our study provides valuable insights into tricuspid valve leaflet remodeling in the
390 context of biventricular heart failure, several limitations warrant consideration. The TIC sheep
391 model replicates key features of biventricular heart failure, but induced disease within weeks
392 rather than years [22]. Therefore, the observed leaflet changes likely reflect early adaptive
393 responses. Although the TIC sheep model successfully induced differential leaflet growth and
394 remodeling, we failed to establish clear correlations between these adaptive responses and
395 potential stimuli like TR severity or right ventricular dilation. Spatial variations in local
396 mechanical properties and strain distributions within each leaflet may influence the expression
397 of remodeling-associated genes and lead to heterogeneous maladaptive responses in VICs
398 across different leaflet regions [31,42]. Beyond our regional immunohistochemistry analysis of
399 cellular remodeling markers, our study did not fully explore the potential impact of mechanical
400 microenvironments within individual leaflets. Additionally, interspecies differences in cardiac
401 structure and response to injury limit the direct translation of these findings to the
402 pathogenesis of functional TR in humans. To overcome these limitations, future studies may
403 explore long-term disease progression models and spatially heterogeneous remodeling
404 responses within tricuspid valve leaflets.

405 **5. CONCLUSION**

406 In conclusion, our study highlights the differential remodeling responses of tricuspid
407 valve leaflets in biventricular heart failure, emphasizing the unique remodeling changes each

408 tricuspid leaflet undergoes. These findings underscore the importance of considering leaflet-
409 specific properties in understanding tricuspid valve dysfunction. By providing insights into how
410 mechanical and cellular factors contribute to these differences, our work paves the way for
411 more targeted and effective interventions in treating tricuspid valve disease.

412 **DATA AVAILABILITY**

413 The data for Figures 1-8 and their appendices are publicly available on the Texas Data
414 Repository https://doi.org/10.18738/T8/5EPBVN. The histology and immunohistochemistry
415 leaflet images are publicly available on the Texas Data Repository
416 https://doi.org/10.18738/T8/2TRJGV.

417 **DISCLOSURE**

418 Manuel K. Rausch has a speaking arrangement with Edwards Lifesciences. The other
419 authors have no conflicts to declare.

420 **AUTHOR CONTRIBUTIONS**

421 **Colton J. Kostelnik:** Investigation, Data curation, Formal analysis, Visualization, Writing -
422 original draft, Writing - review & editing. **William D. Meador:** Conceptualization, Data curation,
423 Software, Formal analysis, Investigation, Methodology, Writing -- original draft, Writing - review
424 & editing. **Chien-Yu Lin:** Investigation, Writing - review & editing. **Mrudang Mathur:**
425 Investigation, Writing - review & editing. **Marcin Malinowski:** Conceptualization, Investigation,
426 Methodology, Writing - review & editing. **Tomasz Jazwiec:** Investigation, Methodology. **Magda**
427 **L Piekarska:** Writing - review & editing. **Boguslaw Gaweda:** Writing - review & editing. **Zuzanna**
428 **Malinowska:** Formal analysis. **Tomasz A. Timek:** Conceptualization, Resources, Supervision,

Funding acquisition, Writing - review & editing. **Manuel K. Rausch:** Conceptualization, Writing - original draft, Writing - review & editing, Supervision, Funding acquisition.

ACKNOWLEDGEMENTS

The research reported in this publication was partially supported by the National Heart, Lung, And Blood Institute of the National Institutes of Health under Award Numbers 1R01HL165251-01 and R21HL161832 (MKR), F31HL145976 (WDM), the American Heart Association for their support under Award Number 18CDA34120028 (MKR), and internal grants from Meijer Heart and Vascular Institute at Corewell Health. The opinions, findings, and conclusions expressed are those of the authors and do not necessarily reflect the official views of the National Institutes of Health or the American Heart Association.

The anterior leaflet data reported in this publication was previously published in [17]. This publication expands upon our earlier work by incorporating additional leaflet comparisons to provide new insights into leaflet-specific remodeling as a response to tachycardia-induced cardiomyopathy.

REFERENCES

[1] J.P. Singh, J.C. Evans, D. Levy, M.G. Larson, L.A. Freed, D.L. Fuller, B. Lehman, E.J. Benjamin, Prevalence and clinical determinants of mitral, tricuspid, and aortic regurgitation (the Framingham Heart Study), The American Journal of Cardiology 83 (1999) 897–902. https://doi.org/10.1016/S0002-9149(98)01064-9.

[2] M. Enriquez-Sarano, D. Messika-Zeitoun, Y. Topilsky, C. Tribouilloy, G. Benfari, H. Michelena, Tricuspid regurgitation is a public health crisis, Progress in Cardiovascular Diseases 62 (2019) 447–451. https://doi.org/10.1016/j.pcad.2019.10.009.

[3] F. Condello, M. Gitto, G.G. Stefanini, Etiology, epidemiology, pathophysiology and management of tricuspid regurgitation: an overview, Reviews in Cardiovascular Medicine 22 (2021) 1115. https://doi.org/10.31083/j.rcm2204122.

[4] E.A. Fender, C.J. Zack, R.A. Nishimura, Isolated tricuspid regurgitation: outcomes and therapeutic interventions, Heart 104 (2018) 798–806. https://doi.org/10.1136/heartjnl-2017-311586.

[5] R.J. Henning, Tricuspid valve regurgitation: current diagnosis and treatment, Am J Cardiovasc Dis. 12 (2022) 1–18.

[6] C.-H. Lee, D.W. Laurence, C.J. Ross, K.E. Kramer, A.R. Babu, E.L. Johnson, M.-C. Hsu, A. Aggarwal, A. Mir, H.M. Burkhart, R.A. Towner, R. Baumwart, Y. Wu, Mechanics of the Tricuspid Valve—From Clinical Diagnosis/Treatment, In-Vivo and In-Vitro Investigations, to Patient-Specific Biomechanical Modeling, Bioengineering 6 (2019) 47. https://doi.org/10.3390/bioengineering6020047.

[7] M. Taramasso, H. Vanermen, F. Maisano, A. Guidotti, G. La Canna, O. Alfieri, The Growing Clinical Importance of Secondary Tricuspid Regurgitation, Journal of the American College of Cardiology 59 (2012) 703–710. https://doi.org/10.1016/j.jacc.2011.09.069.

[8] J.H. Rogers, S.F. Bolling, The Tricuspid Valve: Current Perspective and Evolving Management of Tricuspid Regurgitation, Circulation 119 (2009) 2718–2725. https://doi.org/10.1161/CIRCULATIONAHA.108.842773.

[9] M. Pagnesi, C. Montalto, A. Mangieri, E. Agricola, R. Puri, M. Chiarito, M.B. Ancona, D. Regazzoli, L. Testa, M. De Bonis, N.E. Moat, J. Rodés-Cabau, A. Colombo, A. Latib, Tricuspid annuloplasty versus a conservative approach in patients with functional tricuspid regurgitation undergoing left-sided heart valve surgery: A study-level meta-analysis, International Journal of Cardiology 240 (2017) 138–144. https://doi.org/10.1016/j.ijcard.2017.05.014.

[10] K.J. Grande-Allen, A.G. Borowski, R.W. Troughton, P.L. Houghtaling, N.R. DiPaola, C.S. Moravec, I. Vesely, B.P. Griffin, Apparently normal mitral valves in patients with heart failure demonstrate biochemical and structural derangements, Journal of the American College of Cardiology 45 (2005) 54–61. https://doi.org/10.1016/j.jacc.2004.06.079.

[11] M. Chaput, M.D. Handschumacher, F. Tournoux, L. Hua, J.L. Guerrero, G.J. Vlahakes, R.A. Levine, Mitral Leaflet Adaptation to Ventricular Remodeling: Occurrence and Adequacy in Patients With Functional Mitral Regurgitation, Circulation 118 (2008) 845–852. https://doi.org/10.1161/CIRCULATIONAHA.107.749440.

[12] A. Itoh, G. Krishnamurthy, J.C. Swanson, D.B. Ennis, W. Bothe, E. Kuhl, M. Karlsson, L.R. Davis, D.C. Miller, N.B. Ingels, Active stiffening of mitral valve leaflets in the beating heart, American Journal of Physiology-Heart and Circulatory Physiology 296 (2009) H1766–H1773. https://doi.org/10.1152/ajpheart.00120.2009.

[13] K.J. Grande-Allen, J.E. Barber, K.M. Klatka, P.L. Houghtaling, I. Vesely, C.S. Moravec, P.M. McCarthy, Mitral valve stiffening in end-stage heart failure: Evidence of an organic contribution to functional mitral regurgitation, The Journal of Thoracic and Cardiovascular Surgery 130 (2005) 783–790. https://doi.org/10.1016/j.jtcvs.2005.04.019.

[14] M.K. Rausch, F.A. Tibayan, D. Craig Miller, E. Kuhl, Evidence of adaptive mitral leaflet growth, Journal of the Mechanical Behavior of Biomedical Materials 15 (2012) 208–217. https://doi.org/10.1016/j.jmbbm.2012.07.001.

[15] T.A. Timek, D.T. Lai, P. Dagum, D. Liang, G.T. Daughters, N.B. Ingels, D.C. Miller, Mitral Leaflet Remodeling in Dilated Cardiomyopathy, Circulation 114 (2006). https://doi.org/10.1161/CIRCULATIONAHA.105.000554.

[16] J. Afilalo, J. Grapsa, P. Nihoyannopoulos, J. Beaudoin, J.S.R. Gibbs, R.N. Channick, D. Langleben, L.G. Rudski, L. Hua, M.D. Handschumacher, M.H. Picard, R.A. Levine, Leaflet Area as a Determinant of Tricuspid Regurgitation Severity in Patients With Pulmonary

Hypertension, Circ: Cardiovascular Imaging 8 (2015) e002714. https://doi.org/10.1161/CIRCIMAGING.114.002714.

[17] W.D. Meador, M. Mathur, G.P. Sugerman, M. Malinowski, T. Jazwiec, X. Wang, C.M. Lacerda, T.A. Timek, M.K. Rausch, The tricuspid valve also maladapts as shown in sheep with biventricular heart failure, eLife 9 (2020) e63855. https://doi.org/10.7554/eLife.63855.

[18] A. Iwasieczko, M. Gaddam, B. Gaweda, A. Goodyke, M. Mathur, C.-Y. Lin, J. Zagorski, M. Solarewicz, S. Cohle, M. Rausch, T.A. Timek, Valvular complex and tissue remodelling in ovine functional tricuspid regurgitation, European Journal of Cardio-Thoracic Surgery 63 (2023) ezad115. https://doi.org/10.1093/ejcts/ezad115.

[19] M. Mathur, M. Malinowski, T. Jazwiec, T.A. Timek, M.K. Rausch, Leaflet remodeling reduces tricuspid valve function in a computational model, Journal of the Mechanical Behavior of Biomedical Materials 152 (2024) 106453. https://doi.org/10.1016/j.jmbbm.2024.106453.

[20] M. Mathur, T. Jazwiec, W.D. Meador, M. Malinowski, M. Goehler, H. Ferguson, T.A. Timek, M.K. Rausch, Tricuspid valve leaflet strains in the beating ovine heart, Biomech Model Mechanobiol 18 (2019) 1351–1361. https://doi.org/10.1007/s10237-019-01148-y.

[21] W.D. Meador, M. Mathur, G.P. Sugerman, T. Jazwiec, M. Malinowski, M.R. Bersi, T.A. Timek, M.K. Rausch, A detailed mechanical and microstructural analysis of ovine tricuspid valve leaflets, Acta Biomaterialia 102 (2020) 100–113. https://doi.org/10.1016/j.actbio.2019.11.039.

[22] M. Malinowski, A.G. Proudfoot, D. Langholz, L. Eberhart, M. Brown, H. Schubert, J. Wodarek, T.A. Timek, Large animal model of functional tricuspid regurgitation in pacing induced end-stage heart failure, Interactive CardioVascular and Thoracic Surgery 24 (2017) 905–910. https://doi.org/10.1093/icvts/ivx012.

[23] C.J. Kostelnik, K.J. Crouse, J.D. Goldsmith, J.F. Eberth, Impact of cryopreservation on elastomuscular artery mechanics, Journal of the Mechanical Behavior of Biomedical Materials 154 (2024) 106503. https://doi.org/10.1016/j.jmbbm.2024.106503.

[24] G.A. Duginski, C.J. Ross, D.W. Laurence, C.H. Johns, C.-H. Lee, An investigation of the effect of freezing storage on the biaxial mechanical properties of excised porcine tricuspid valve anterior leaflets, Journal of the Mechanical Behavior of Biomedical Materials 101 (2020) 103438. https://doi.org/10.1016/j.jmbbm.2019.103438.

[25] K.J. Smith, M. Mathur, W.D. Meador, B. Phillips-Garcia, G.P. Sugerman, A.K. Menta, T. Jazwiec, M. Malinowski, T.A. Timek, M.K. Rausch, Tricuspid Chordae Tendineae Mechanics: Insertion Site, Leaflet, and Size-Specific Analysis and Constitutive Modelling, Exp Mech 61 (2021) 19–29. https://doi.org/10.1007/s11340-020-00594-5.

[26] W.D. Meador, J. Zhou, M. Malinowski, T. Jazwiec, S. Calve, T.A. Timek, M.K. Rausch, The effects of a simple optical clearing protocol on the mechanics of collagenous soft tissue, Journal of Biomechanics 122 (2021) 110413. https://doi.org/10.1016/j.jbiomech.2021.110413.

[27] A.J. Schriefl, A.J. Reinisch, S. Sankaran, D.M. Pierce, G.A. Holzapfel, Quantitative assessment of collagen fibre orientations from two-dimensional images of soft biological tissues, J. R. Soc. Interface. 9 (2012) 3081–3093. https://doi.org/10.1098/rsif.2012.0339.

[28] M.S. Sacks, Biaxial Mechanical Evaluation of Planar Biological Materials, in: S.C. Cowin, J.D. Humphrey (Eds.), Cardiovascular Soft Tissue Mechanics, Kluwer Academic Publishers, Dordrecht, 2004: pp. 199–246. https://doi.org/10.1007/0-306-48389-0_7.

[29] K.M. Kodigepalli, K. Thatcher, T. West, D.P. Howsmon, F.J. Schoen, M.S. Sacks, C.K. Breuer, J. Lincoln, Biology and Biomechanics of the Heart Valve Extracellular Matrix, JCDD 7 (2020) 57. https://doi.org/10.3390/jcdd7040057.

[30] L.T. Hudson, S.V. Jett, K.E. Kramer, D.W. Laurence, C.J. Ross, R.A. Towner, R. Baumwart, K.M. Lim, A. Mir, H.M. Burkhart, Y. Wu, C.-H. Lee, A Pilot Study on Linking Tissue Mechanics with Load-Dependent Collagen Microstructures in Porcine Tricuspid Valve Leaflets, Bioengineering 7 (2020) 60. https://doi.org/10.3390/bioengineering7020060.

[31] D. Laurence, C. Ross, S. Jett, C. Johns, A. Echols, R. Baumwart, R. Towner, J. Liao, P. Bajona, Y. Wu, C.-H. Lee, An investigation of regional variations in the biaxial mechanical properties and stress relaxation behaviors of porcine atrioventricular heart valve leaflets, Journal of Biomechanics 83 (2019) 16–27. https://doi.org/10.1016/j.jbiomech.2018.11.015.

[32] T.L. Blevins, S.B. Peterson, E.L. Lee, A.M. Bailey, J.D. Frederick, T.N. Huynh, V. Gupta, K.J. Grande-Allen, Mitral Valvular Interstitial Cells Demonstrate Regional, Adhesional, and Synthetic Heterogeneity, Cells Tissues Organs 187 (2008) 113–122. https://doi.org/10.1159/000108582.

[33] H. Ma, A.R. Killaars, F.W. DelRio, C. Yang, K.S. Anseth, Myofibroblastic activation of valvular interstitial cells is modulated by spatial variations in matrix elasticity and its organization, Biomaterials 131 (2017) 131–144. https://doi.org/10.1016/j.biomaterials.2017.03.040.

[34] G.A. Walker, K.S. Masters, D.N. Shah, K.S. Anseth, L.A. Leinwand, Valvular Myofibroblast Activation by Transforming Growth Factor-β: Implications for Pathological Extracellular Matrix Remodeling in Heart Valve Disease, Circulation Research 95 (2004) 253–260. https://doi.org/10.1161/01.RES.0000136520.07995.aa.

[35] Y. Li, K.O. Lui, B. Zhou, Reassessing endothelial-to-mesenchymal transition in cardiovascular diseases, Nat Rev Cardiol 15 (2018) 445–456. https://doi.org/10.1038/s41569-018-0023-y.

[36] K.J. Grande-Allen, J. Liao, The Heterogeneous Biomechanics and Mechanobiology of the Mitral Valve: Implications for Tissue Engineering, Curr Cardiol Rep 13 (2011) 113–120. https://doi.org/10.1007/s11886-010-0161-2.

[37] J.P. Dal-Bianco, E. Aikawa, J. Bischoff, J.L. Guerrero, M.D. Handschumacher, S. Sullivan, B. Johnson, J.S. Titus, Y. Iwamoto, J. Wylie-Sears, R.A. Levine, A. Carpentier, Active Adaptation of the Tethered Mitral Valve: Insights Into a Compensatory Mechanism for Functional Mitral Regurgitation, Circulation 120 (2009) 334–342. https://doi.org/10.1161/CIRCULATIONAHA.108.846782.

[38] S. Korossis, Structure-Function Relationship of Heart Valves in Health and Disease, in: K. Kirali (Ed.), Structural Insufficiency Anomalies in Cardiac Valves, InTech, 2018. https://doi.org/10.5772/intechopen.78280.

[39] T. Jazwiec, M.J. Malinowski, H. Ferguson, J. Parker, M. Mathur, M.K. Rausch, T.A. Timek, Tricuspid Valve Anterior Leaflet Strains in Ovine Functional Tricuspid Regurgitation,

Seminars in Thoracic and Cardiovascular Surgery 33 (2021) 356–364. https://doi.org/10.1053/j.semtcvs.2020.09.012.

[40] A. Iwasieczko, T. Jazwiec, M. Gaddam, B. Gaweda, M. Piekarska, M. Solarewicz, M.K. Rausch, T.A. Timek, Septal annular dilation in chronic ovine functional tricuspid regurgitation, The Journal of Thoracic and Cardiovascular Surgery 166 (2023) e393–e403. https://doi.org/10.1016/j.jtcvs.2023.04.003.

[41] C.E. Haese, M. Mathur, C.-Y. Lin, M. Malinowski, T.A. Timek, M.K. Rausch, Impact of tricuspid annuloplasty device shape and size on valve mechanics—a computational study, JTCVS Open 17 (2024) 111–120. https://doi.org/10.1016/j.xjon.2023.11.002.

[42] K.E. Kramer, C.J. Ross, D.W. Laurence, A.R. Babu, Y. Wu, R.A. Towner, A. Mir, H.M. Burkhart, G.A. Holzapfel, C.-H. Lee, An investigation of layer-specific tissue biomechanics of porcine atrioventricular valve anterior leaflets, Acta Biomaterialia 96 (2019) 368–384. https://doi.org/10.1016/j.actbio.2019.06.049.

601 **FIGURES**

602 **Figure 1**

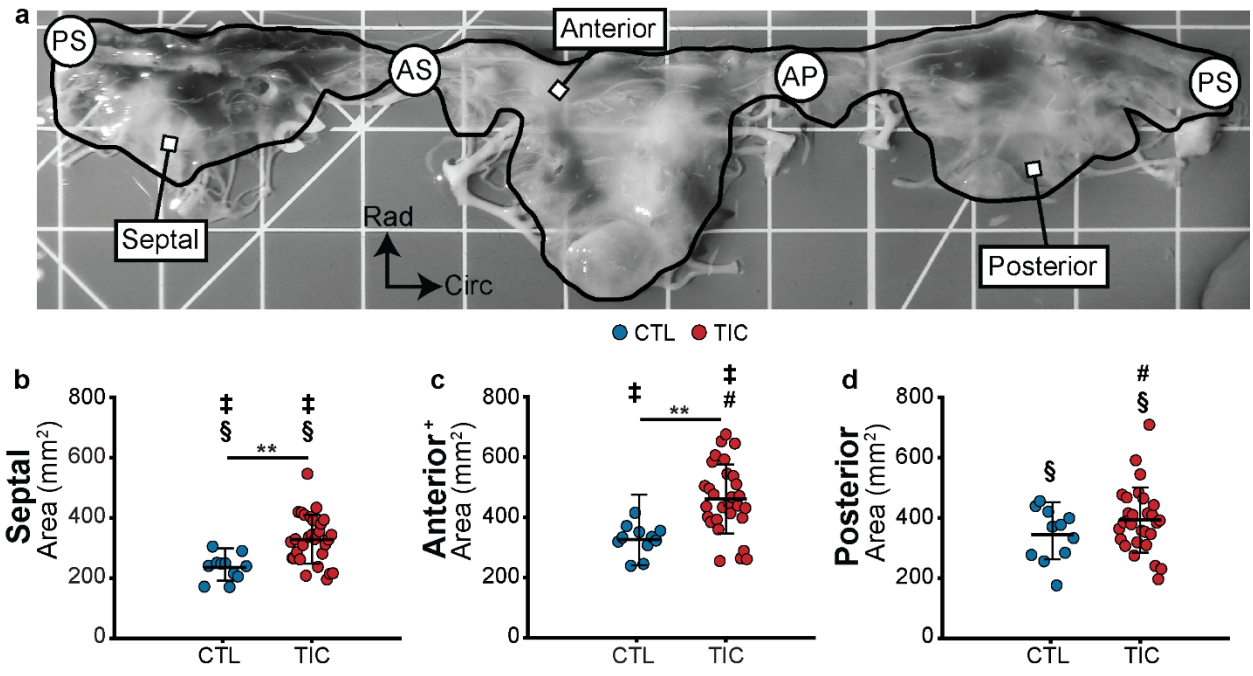

603

604

605 **Figure 2**

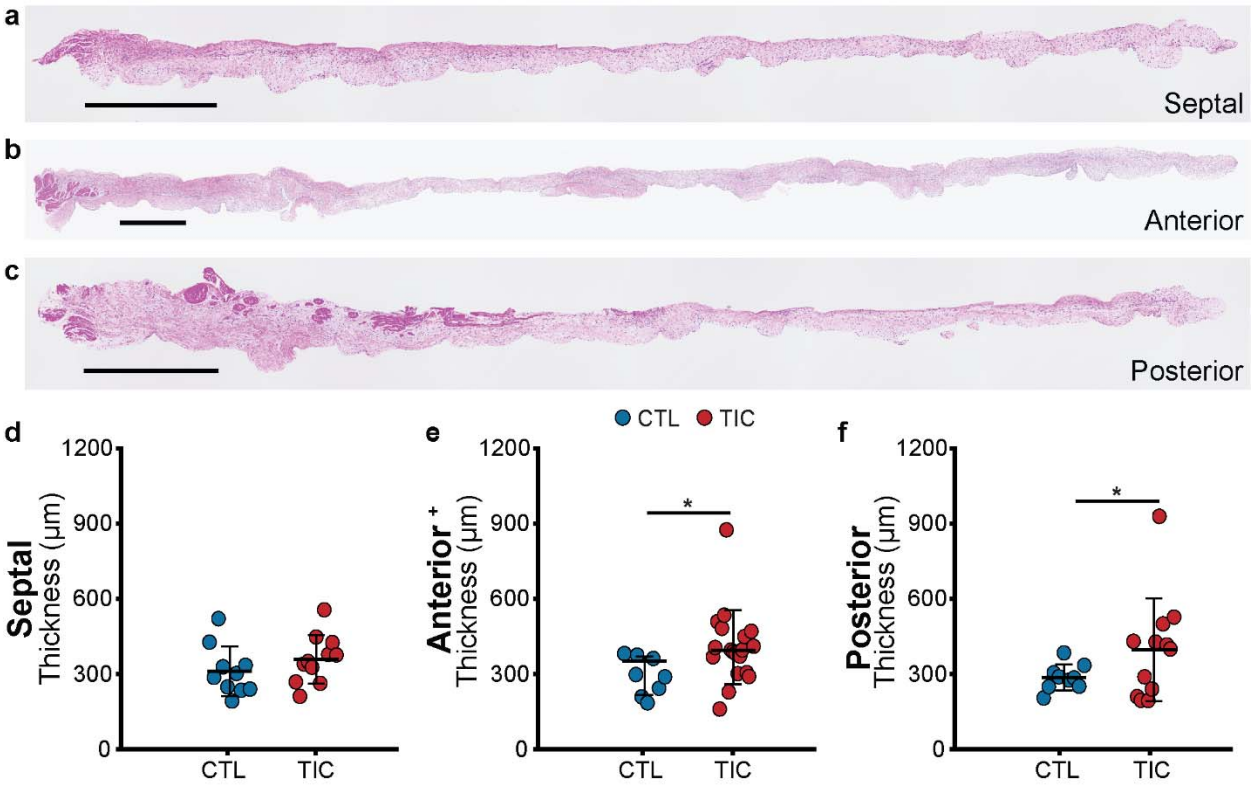

606

607

608 **Figure 3**

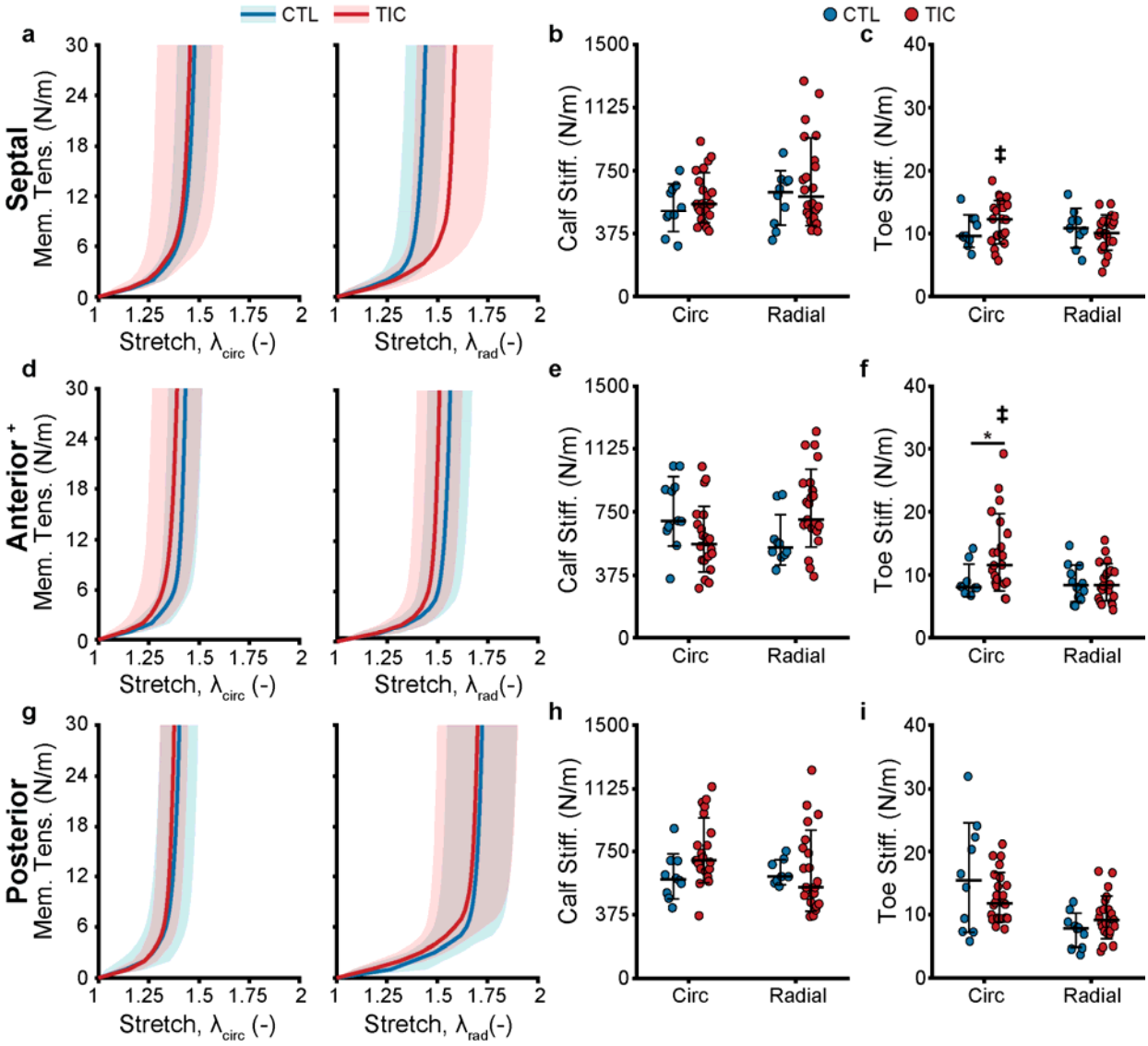

609

610

611 **Figure 4**

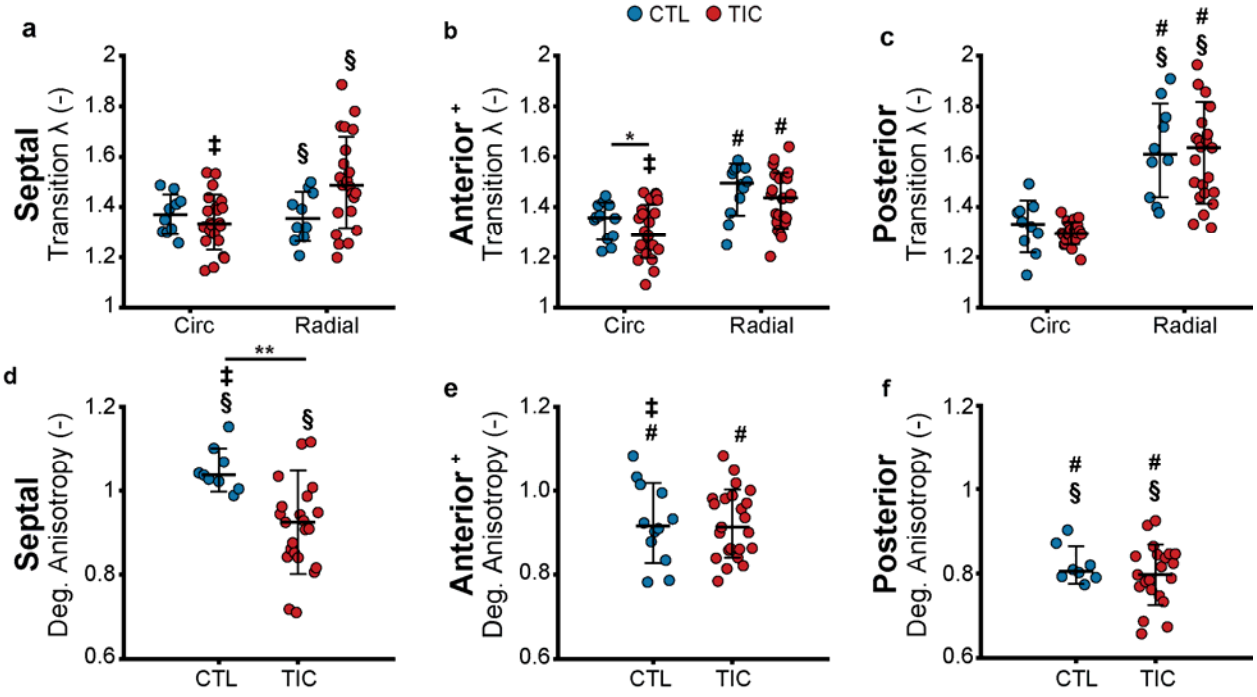

612

613

Figure 5

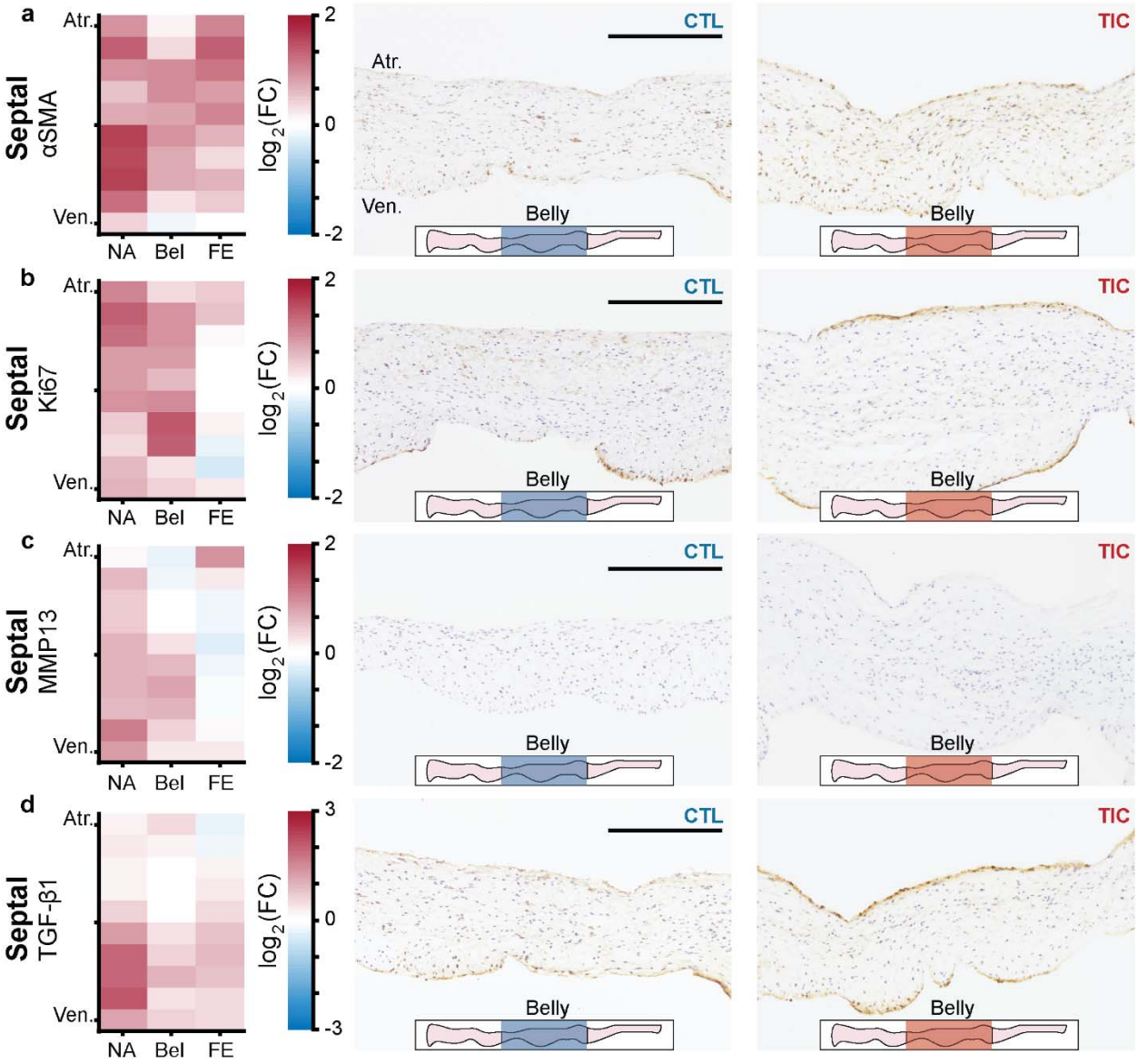
a
Atr.
Septal
αSMA
Ven.
NA
Bel
FE
log2(FC)
2
0
-2
CTL
Atr.
Ven.
Belly
TIC
Belly
b
Atr.
Septal
Ki67
Ven.
NA
Bel
FE
log2(FC)
2
0
-2
CTL
Belly
TIC
Belly
c
Atr.
Septal
MMP13
Ven.
NA
Bel
FE
log2(FC)
2
0
-2
CTL
Belly
TIC
Belly
d
Atr.
Septal
TGF-β1
Ven.
NA
Bel
FE
log2(FC)
3
0
-3
CTL
Belly
TIC
Belly

617 **Figure 6**

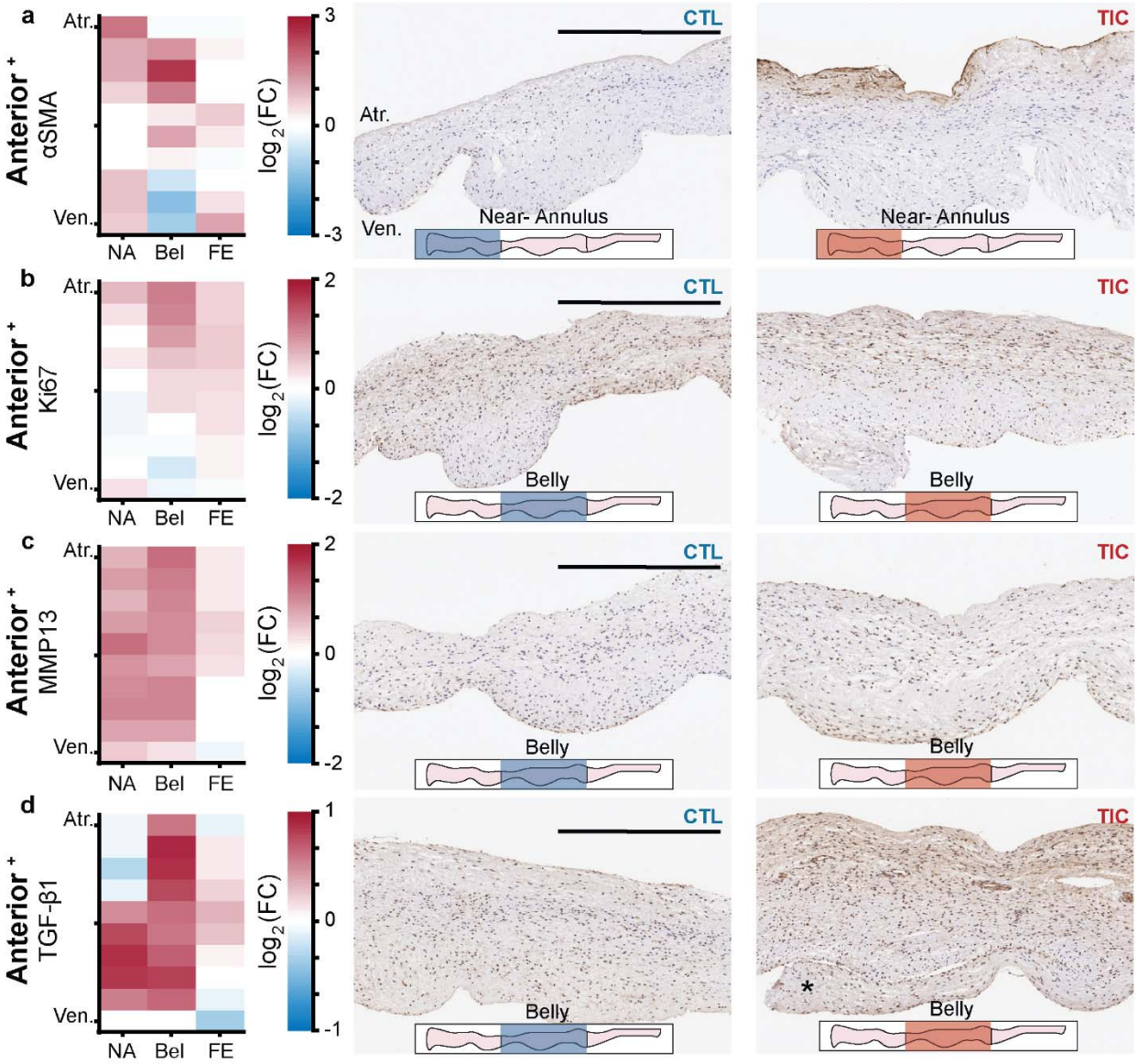

618

619

620 **Figure 7**

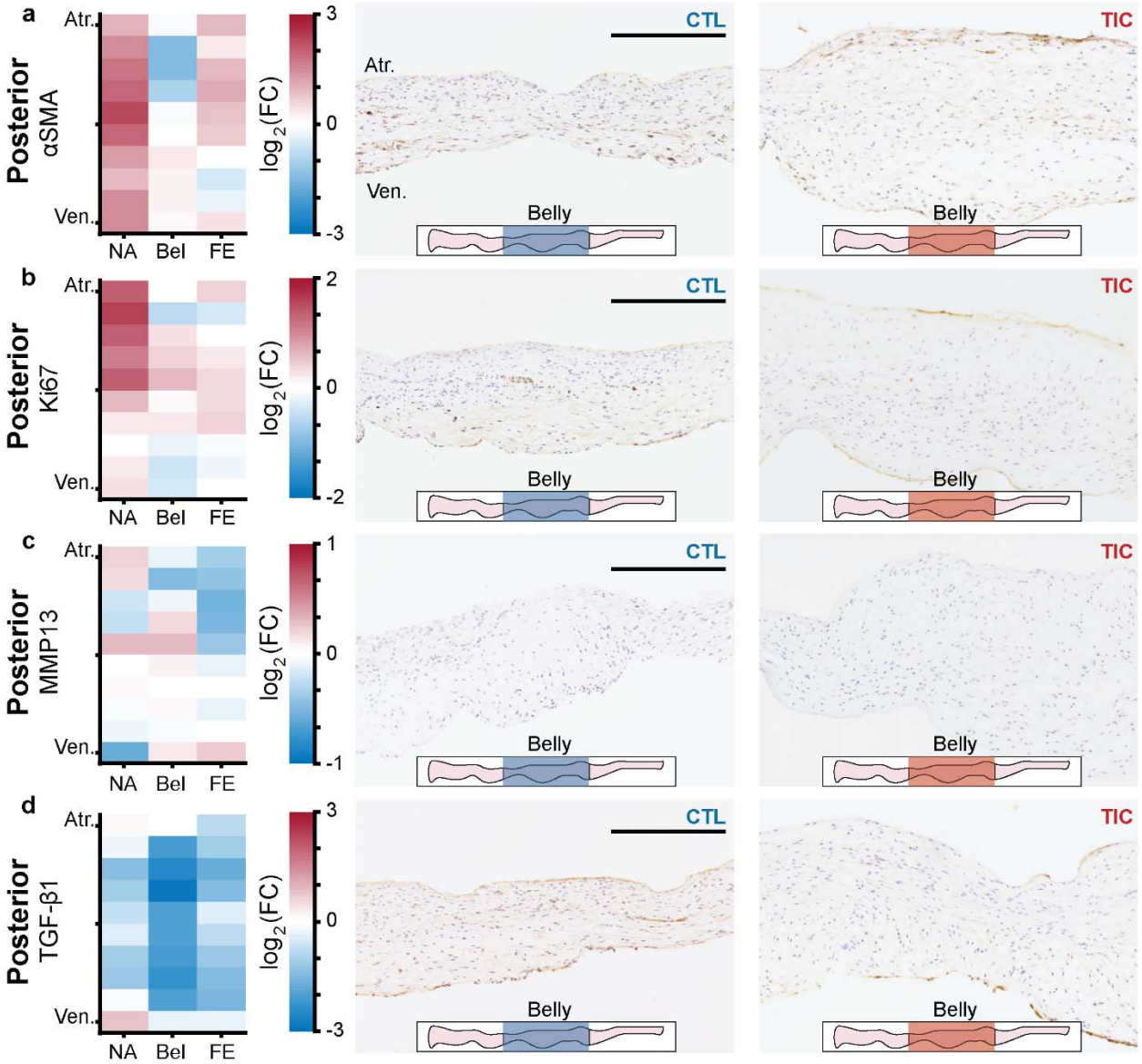

621

622

Figure 8

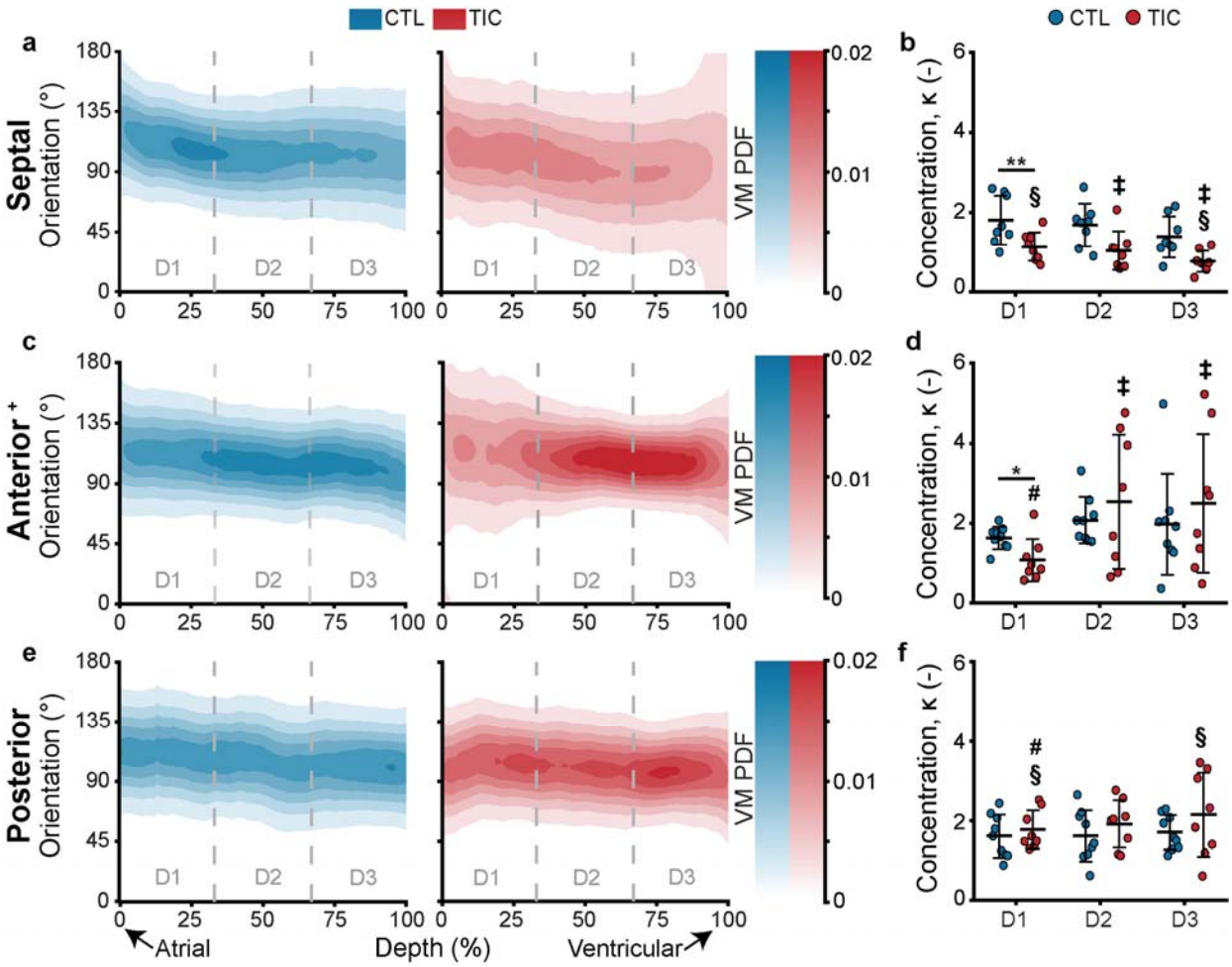
CTL
TIC
a
b
c
d
e
f
Septal
Anterior+
Posterior
Orientation (°)
Concentration, κ (-)
VM PDF
D1
D2
D3
Atrial
Depth (%)
Ventricular

627 **TABLES**

628 **Table 1**

Parameter	CTL	TIC (baseline)	TIC (terminal)
Echocardiographic data			
TR grade	1.0 (0.0)	0.0 (0.0)	2.0 (1.0) * †
RV EF, %	67.0 ± 8.6	58.8 (20.5)	48.4 ± 12.9 * †
RV FAC, %	52.1 ± 6.0	53.9 ± 8.0	37.4 ± 8.7 * †
RV IDd, cm	2.5 ± 0.4	2.6 (0.6)	2.9 ± 0.7 *
TV annulus dimension, cm	2.5 (0.3)	2.5 ± 0.4	3.2 ± 0.5 * †
MR grade	0.0 (0.0)	0.0 (0.0)	2.0 (1.0) * †
LV EF, %	55.8 ± 4.4	61.3 ± 6.2	30.0 (11.2) * †
LV IDd, cm	4.2 ± 0.3	3.7 ± 0.6	4.6 ± 0.4 * †
Hemodynamic data			
HR, bpm	108 (11)	-	126 ± 23 *
RV P_{Max}, mmHg	28.8 (11.4)	-	44.0 ± 11.5 *
RV P_{ES}, mmHg	22.3 ± 5.6	-	35.7 ± 11.0 *
RA P_{Mean}, mmHg	10.5 (3.2)	-	10.6 (5.6)
LV P_{Max}, mmHg	96.1 ± 9.7	-	92.9 ± 13.8
LV P_{ES}, mmHg	63.1 ± 17.8	-	64.4 ± 13.6

Values are mean ± standard deviation or median (interquartile range).
CTL = control, EF = ejection fraction, ES = end systolic, FAC = fractional area change, HR = heart rate, IDd = inner dimension at diastole, LV = left ventricular, Max = maximal, MR = mitral regurgitation, P = pressure, RA = right atrial, RV = right ventricular, TIC = tachycardia-induced cardiomyopathy, TR = tricuspid regurgitation, TV = tricuspid valve.
* $p < 0.05$ vs. CTL, † $p < 0.05$ vs TIC (baseline)

629

630 **CAPTIONS**

631 **Figure 1:** Tricuspid septal and anterior leaflet area increases in sheep with tachycardia-induced
632 cardiomyopathy (TIC). (a) Sheep tricuspid valve image on a calibrated grid (1 cm scale).
633 Measured areas (black line) of septal, anterior, and posterior leaflets are shown. Leaflet areas
634 were measured between commissures: posterior-septal (PS) to antero-septal (AS) for septal, AS
635 to antero-posterior (AP) for anterior, and AP to PS for posterior. (b-d) Leaflet area comparisons
636 between control (CTL, blue, n = 12) and TIC (red, n = 29) for septal, anterior, and posterior
637 leaflets. The (+) indicates that the anterior leaflet data was previously published and can be
638 found in [17]. Statistical significance between animal group (CTL vs. TIC) is denoted by (**) for p
639 < 0.01 using one-tailed pairwise tests. Statistical significance between leaflets is denoted by (‡)
640 for septal vs. anterior, (#) for anterior vs. posterior, and (§) for septal vs. posterior, all at p ≤
641 0.0001, using two-tailed pairwise tests.

642 **Figure 2:** Tricuspid anterior and posterior leaflet thickness increases in sheep with tachycardia-
643 induced cardiomyopathy (TIC). Representative images of (a) septal, (b) anterior, and (c)
644 posterior leaflet strips. Averaged thickness comparisons between control (CTL, blue, n = 8-10)
645 and TIC (red, n = 11-12) (d) septal, (e) anterior, and (f) posterior leaflets. The (+) indicates that
646 the anterior leaflet data was previously published and can be found in [17]. Statistical
647 significance between animal group (CTL vs. TIC) is denoted by (*) for p < 0.05 using one-tailed
648 pairwise tests.

649 **Figure 3:** Tachycardia-induced cardiomyopathy (TIC) anterior leaflets are stiffer at low stretches
650 in the circumferential (circ) directions. Control (CTL, blue, n = 10 for each leaflet) and TIC (red, n
651 = 22 for each leaflet) membrane tension (Mem. Tens.) vs stretch average curves (solid) with

652 standard deviation (shaded) in the circumferential and radial (rad) directions for (a) posterior
653 and (d) septal leaflets. Comparisons of the (b & e) stiffness at large stretches (calf stiffness) in
654 the circumferential and radial directions for the posterior and septal leaflets, respectively.
655 Comparisons of the (c & f) stiffness at small stretches (toe stiffness) in the circumferential and
656 radial directions for the posterior and septal leaflets, respectively. The (+) indicates that the
657 anterior leaflet data was previously published and can be found in [17]. Statistical significance
658 between animal group (CTL vs. TIC) is denoted by (*) using one-tailed pairwise tests at $p < 0.05$,
659 and statistical significance between septal and anterior leaflets is denoted by (‡) using two-
660 tailed pairwise tests at $p < 0.05$.

661 **Figure 4:** Tachycardia-induced cardiomyopathy (TIC) septal leaflets exhibit increased radial
662 transition stretch and decreased anisotropy. Comparisons of the transition stretch in
663 circumferential and radial directions between control (CTL, blue, n = 10) and TIC (red, n = 22) (a)
664 septal, (b) anterior, and (c) posterior leaflets. Comparisons of the degree of anisotropy between
665 CTL (blue, n = 10) and TIC (red, n = 22) (d) septal, (e) anterior, and (f) posterior leaflets. The (+)
666 indicates that the anterior leaflet data was previously published and can be found in [17].
667 Statistical significance between animal group (CTL vs. TIC) is denoted by (*) for $p < 0.05$ and (**)
668 for $p < 0.01$ using one-tailed pairwise tests. Statistical significance between leaflets is denoted
669 by (‡) for septal vs. anterior, (#) for anterior vs. posterior, and (§) for septal vs. posterior, all at p
670 < 0.05, using two-tailed pairwise tests.

671 **Figure 5:** Changes in remodeling cellular markers in tachycardia-induced cardiomyopathy (TIC)
672 septal leaflets. (a-d) Heat maps (left) showing regional expression of (a) alpha-smooth muscle
673 actin (α-SMA), (b) Ki67, (c) matrix metalloproteinase 13 (MMP13), (d) transforming growth

674 factor beta (TGF-β1). The heatmaps are separated into three equidistant regions along the
675 radial axis (near-annulus (NA), belly (Bel), free edge (FE)) and 10 thickness regions from the
676 atrial surface (Atr.) to the ventricular surface (Ven.). Fold change (FC) between control (CTL, n =
677 6) and TIC (n = 6) was determined by the ratio of positively stained pixel percentage between
678 TIC and CTL. Color map indicates the logarithm base 2 of the fold change, interpreted as
679 (positive, red): TIC expression is higher than CTL, (0, white): TIC and CTL expression are
680 approximately equal, and (negative, blue): TIC expression is less than CTL. Representative
681 images of CTL (middle) and TIC (right) posterior leaflets are shown with the atrial surface
682 upward. The inset leaflet schematic depicts the longitudinal region from which the
683 representative image was taken. Scale bars = 500 μm.

684 **Figure 6:** Changes in remodeling cellular markers in tachycardia-induced cardiomyopathy (TIC)
685 anterior leaflets. The (+) indicates that the anterior leaflet data was previously published and
686 can be found in [17]. (a-d) Heat maps (left) showing regional expression of (a) alpha-smooth
687 muscle actin (α-SMA), (b) Ki67, (c) matrix metalloproteinase 13 (MMP13), (d) transforming
688 growth factor beta (TGF-β1). The heatmaps are separated into three equidistant regions along
689 the radial axis (near-annulus (NA), belly (Bel), free edge (FE)) and 10 thickness regions from the
690 atrial surface (Atr.) to the ventricular surface (Ven.). Fold change (FC) between control (CTL, n =
691 6) and TIC (n = 6) was determined by the ratio of positively stained pixel percentage between
692 TIC and CTL. Color map indicates the logarithm base 2 of the fold change, interpreted as
693 (positive, red): TIC expression is higher than CTL, (0, white): TIC and CTL expression are
694 approximately equal, and (negative, blue): TIC expression is less than CTL. Representative
695 images of CTL (middle) and TIC (right) posterior leaflets are shown with the atrial surface

696 upward. The inset leaflet schematic depicts the longitudinal region from which the
697 representative image was taken. Scale bars = 500 μm.

698 **Figure 7:** Changes in remodeling cellular markers in tachycardia-induced cardiomyopathy (TIC)
699 posterior leaflets. (a-d) Heat maps (left) showing regional expression of (a) alpha-smooth
700 muscle actin (α-SMA), (b) Ki67, (c) matrix metalloproteinase 13 (MMP13), (d) transforming
701 growth factor beta (TGF-β1). The heatmaps are separated into three equidistant regions along
702 the radial axis (near-annulus (NA), belly (Bel), free edge (FE)) and 10 thickness regions from the
703 atrial surface (Atr.) to the ventricular surface (Ven.). Fold change (FC) between control (CTL, n =
704 6) and TIC (n = 6) was determined by the ratio of positively stained pixel percentage between
705 TIC and CTL. Color map indicates the logarithm base 2 of the fold change, interpreted as
706 (positive, red): TIC expression is higher than CTL, (0, white): TIC and CTL expression are
707 approximately equal, and (negative, blue): TIC expression is less than CTL. Representative
708 images of CTL (middle) and TIC (right) posterior leaflets are shown with the atrial surface
709 upward. The inset leaflet schematic depicts the longitudinal region from which the
710 representative image was taken. Scale bars = 500 μm.

711 **Figure 8:** Through-depth collagen microstructure reveals similar mean orientations and regional
712 concentration changed throughout depth between control (CTL) and tachycardia-induced
713 cardiomyopathy (TIC) tricuspid leaflets. Heat map visualizations of von Mises probability
714 distribution functions (VM PDF) fit to collagen fiber orientation histograms of two-photon
715 acquired images throughout the entire depth (0% - Atrial surface, 100% - Ventricular surface) of
716 averaged CTL (blue, n = 9 for each leaflet) and TIC (red, n = 9 for each leaflet) (a) septal, (c)
717 anterior, (e) posterior leaflets. Comparisons of VM concentration parameter, κ, across depth

718 regions D1, D2, and D3 for the (b) septal, (d) anterior, and (f) posterior leaflets. The (+) indicates
719 that the anterior leaflet data was previously published and can be found in [17]. Statistical
720 significance between animal group (CTL vs. TIC) is denoted by (*) for $p < 0.05$ and (**) for $p <$
721 0.01 using one-tailed pairwise tests. Statistical significance between leaflets is denoted by (‡)
722 for septal vs. anterior, (#) for anterior vs. posterior, and (§) for septal vs. posterior, all at $p <$
723 0.05, using two-tailed pairwise tests.
724
725 **Table 1:** Echocardiographic and hemodynamic data of animal model.

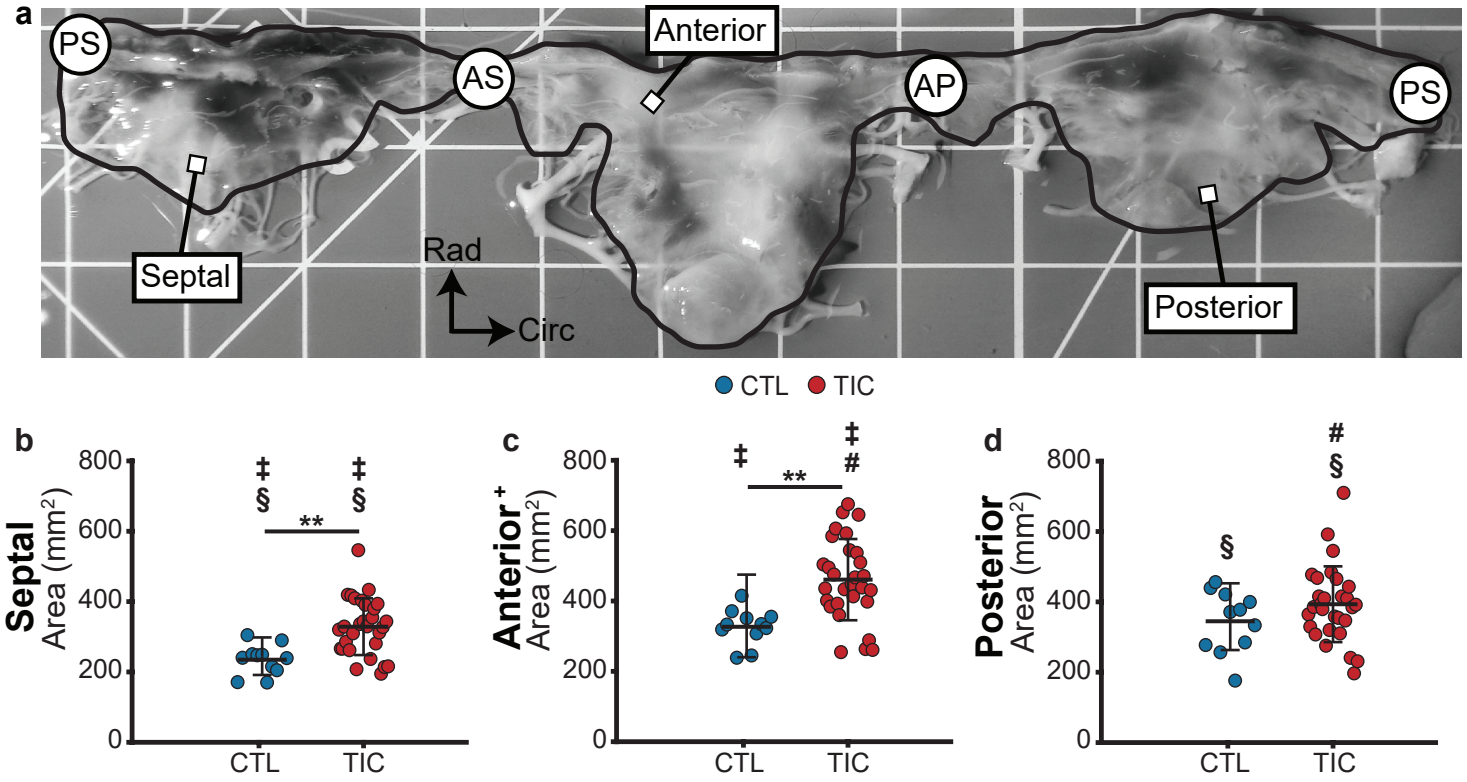
a
PS
AS
Anterior
AP
PS
Septal
Rad
Circ
Posterior
CTL
TIC
b
Septal
Area (mm²)
800
600
400
200
0
‡
§
‡
§
**
CTL
TIC
c
Anterior⁺
Area (mm²)
800
600
400
200
0
‡
‡
#
**
CTL
TIC
d
Posterior
Area (mm²)
800
600
400
200
0
§
#
§
CTL
TIC

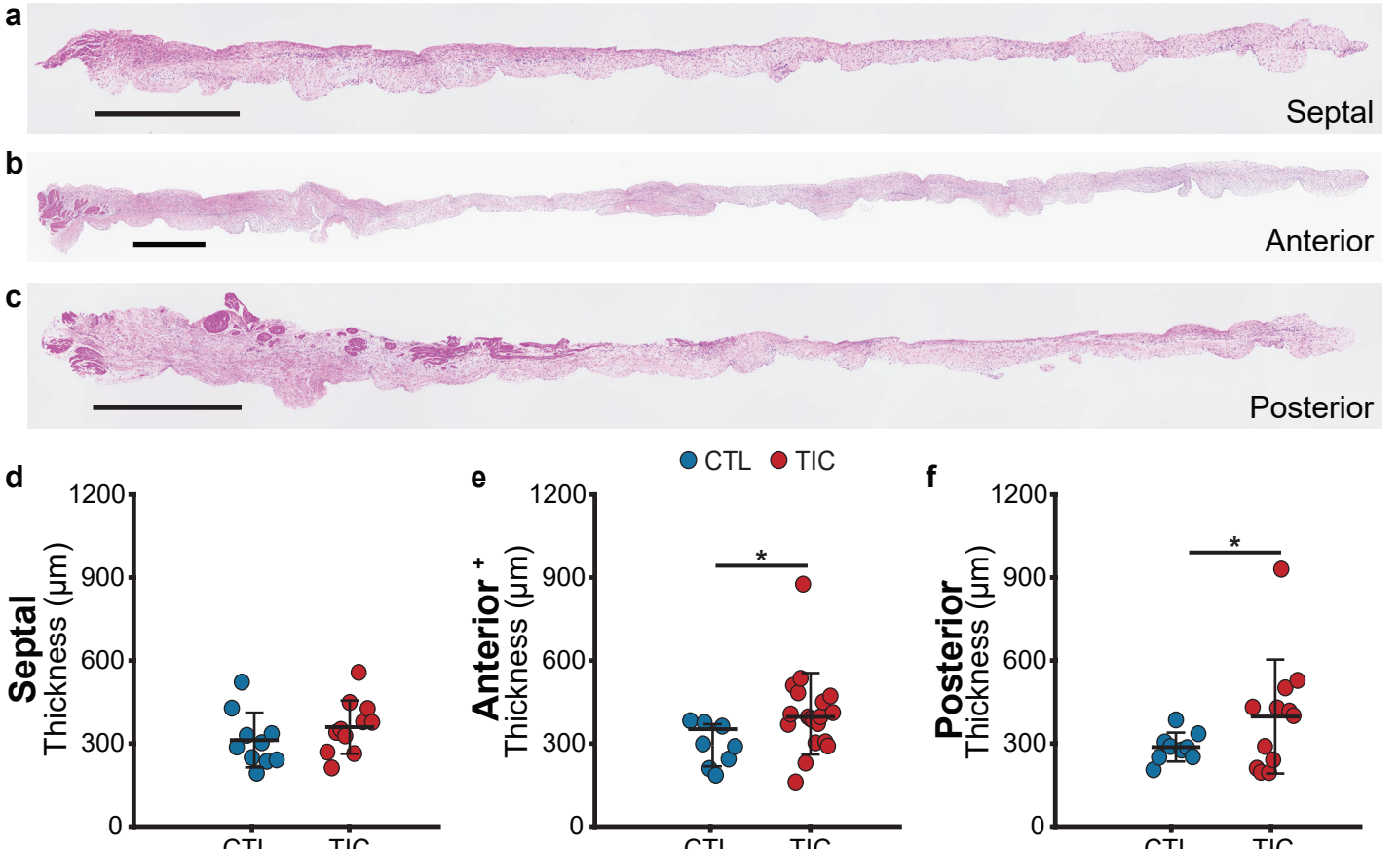
a
Septal
b
Anterior
c
Posterior
CTL
TIC
d
Septal
Thickness (µm)
1200
900
600
300
0
CTL
TIC
e
Anterior +
Thickness (µm)
*
f
Posterior
Thickness (µm)
*

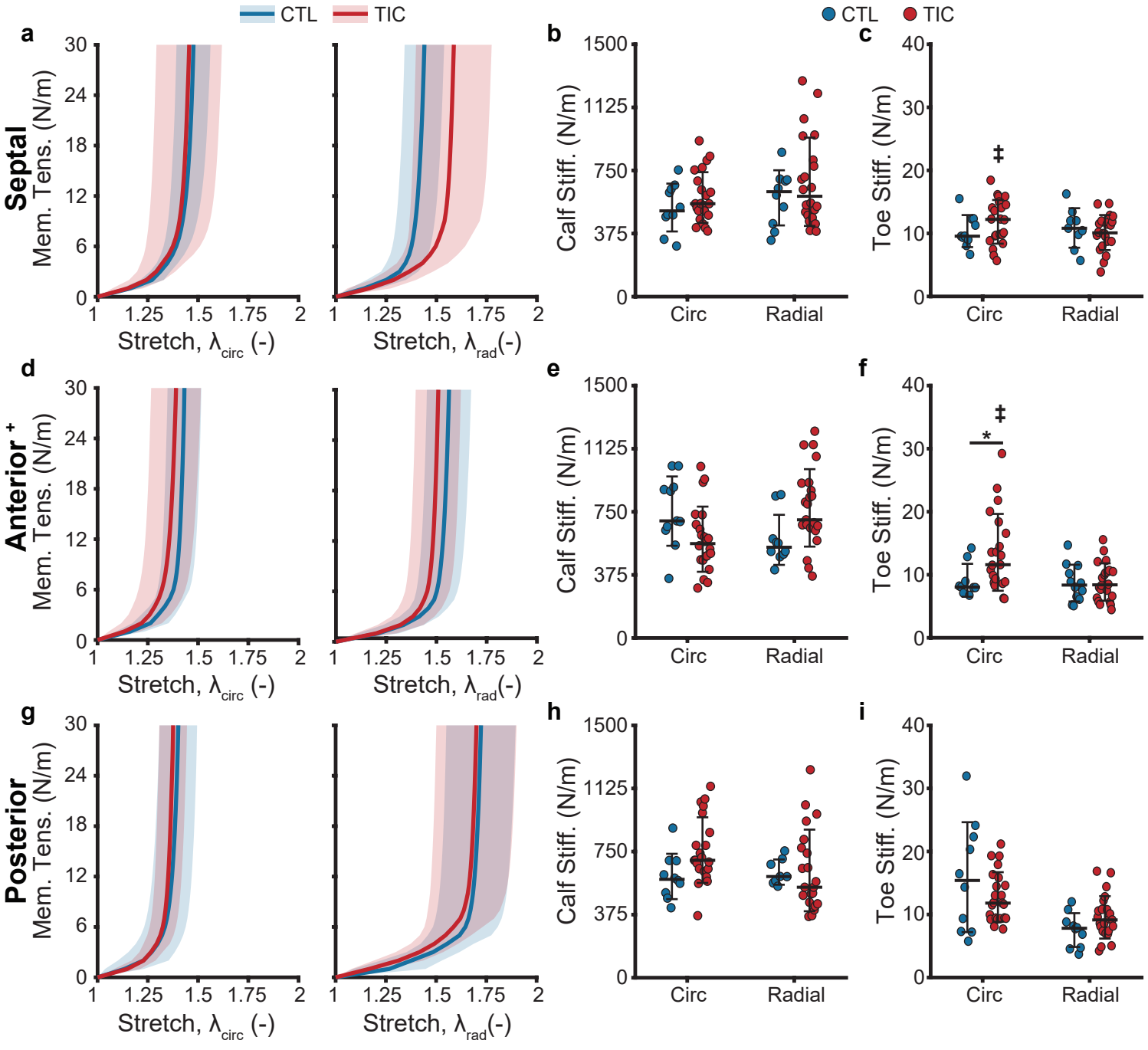
CTL
TIC
a
b
c
d
e
f
g
h
i
Septal
Anterior +
Posterior
Mem. Tens. (N/m)
Stretch, λcirc (-)
Stretch, λrad(-)
Calf Stiff. (N/m)
Toe Stiff. (N/m)
Circ
Radial
*
‡

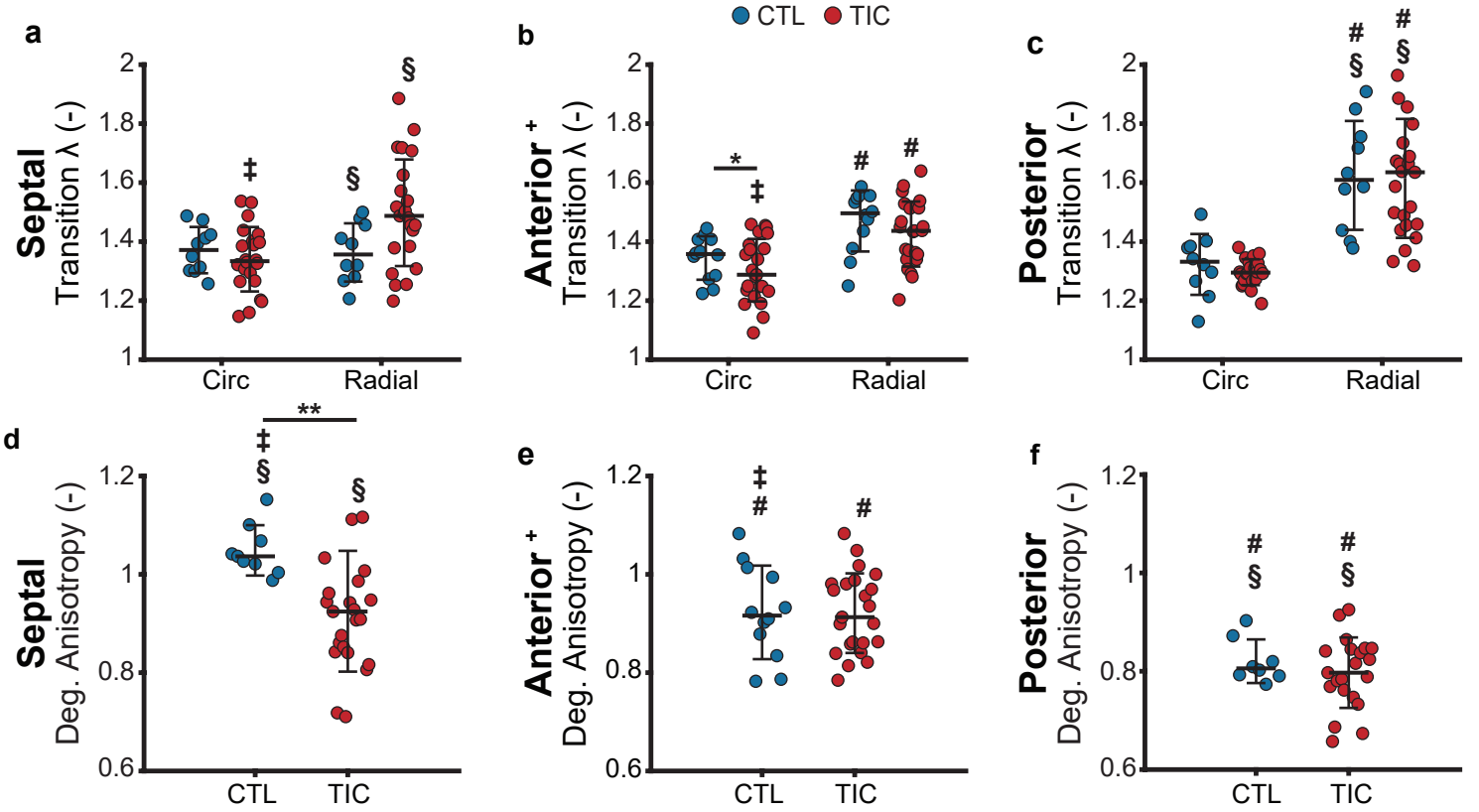
CTL
TIC
a
Septal
Transition λ (-)
2
1.8
1.6
1.4
1.2
1
‡
§
§
Circ
Radial
b
Anterior +
Transition λ (-)
*
‡
#
#
c
Posterior
Transition λ (-)
#
§
#
§
d
Septal
Deg. Anisotropy (-)
1.2
1
0.8
0.6
**
‡
§
§
CTL
TIC
e
Anterior +
Deg. Anisotropy (-)
‡
#
#
f
Posterior
Deg. Anisotropy (-)
#
§
#
§

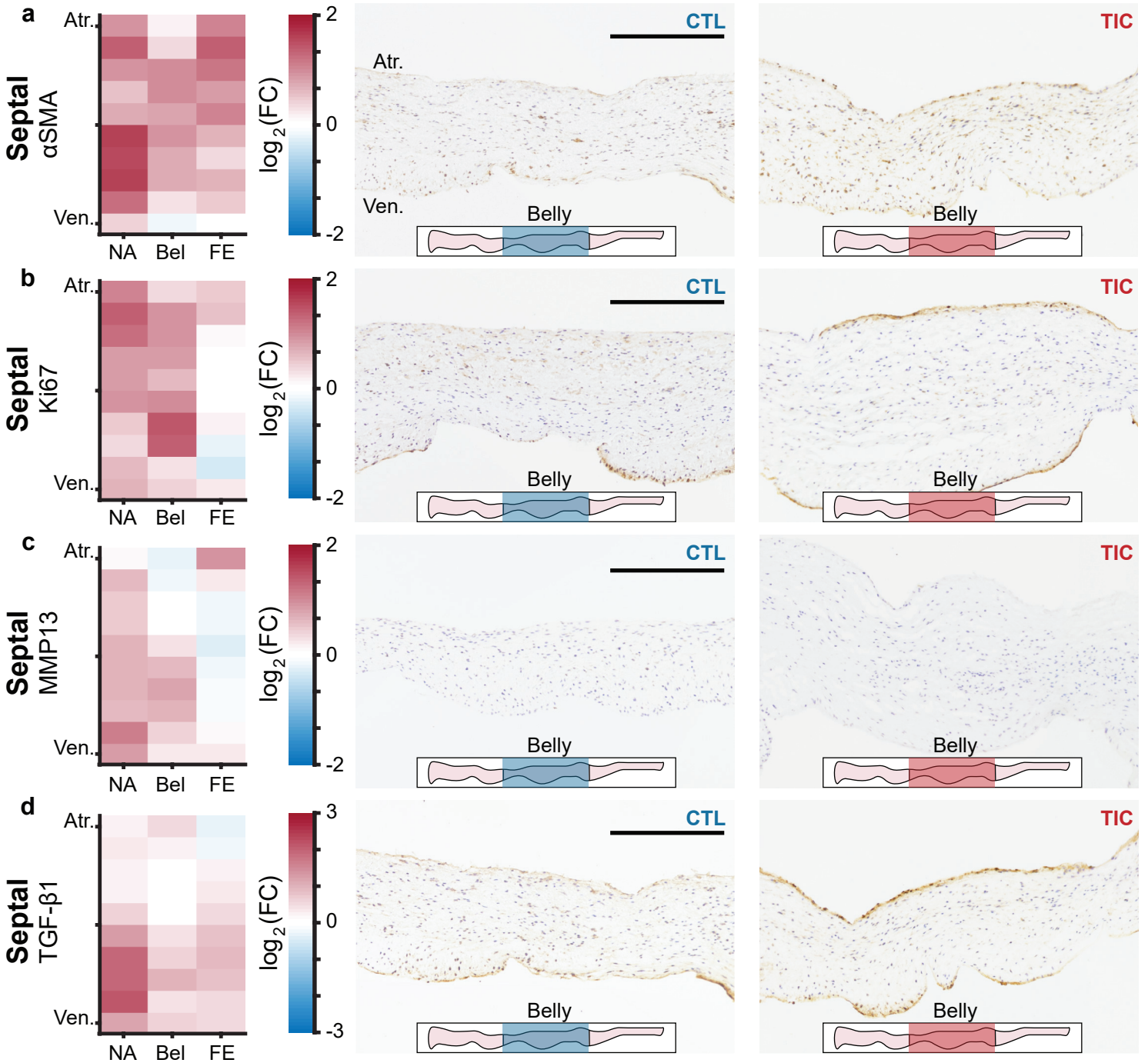
a
Septal
αSMA
Atr.
Ven.
NA
Bel
FE
log2(FC)
2
0
-2
CTL
TIC
Atr.
Ven.
Belly
b
Septal
Ki67
c
Septal
MMP13
d
Septal
TGF-β1
3
-3

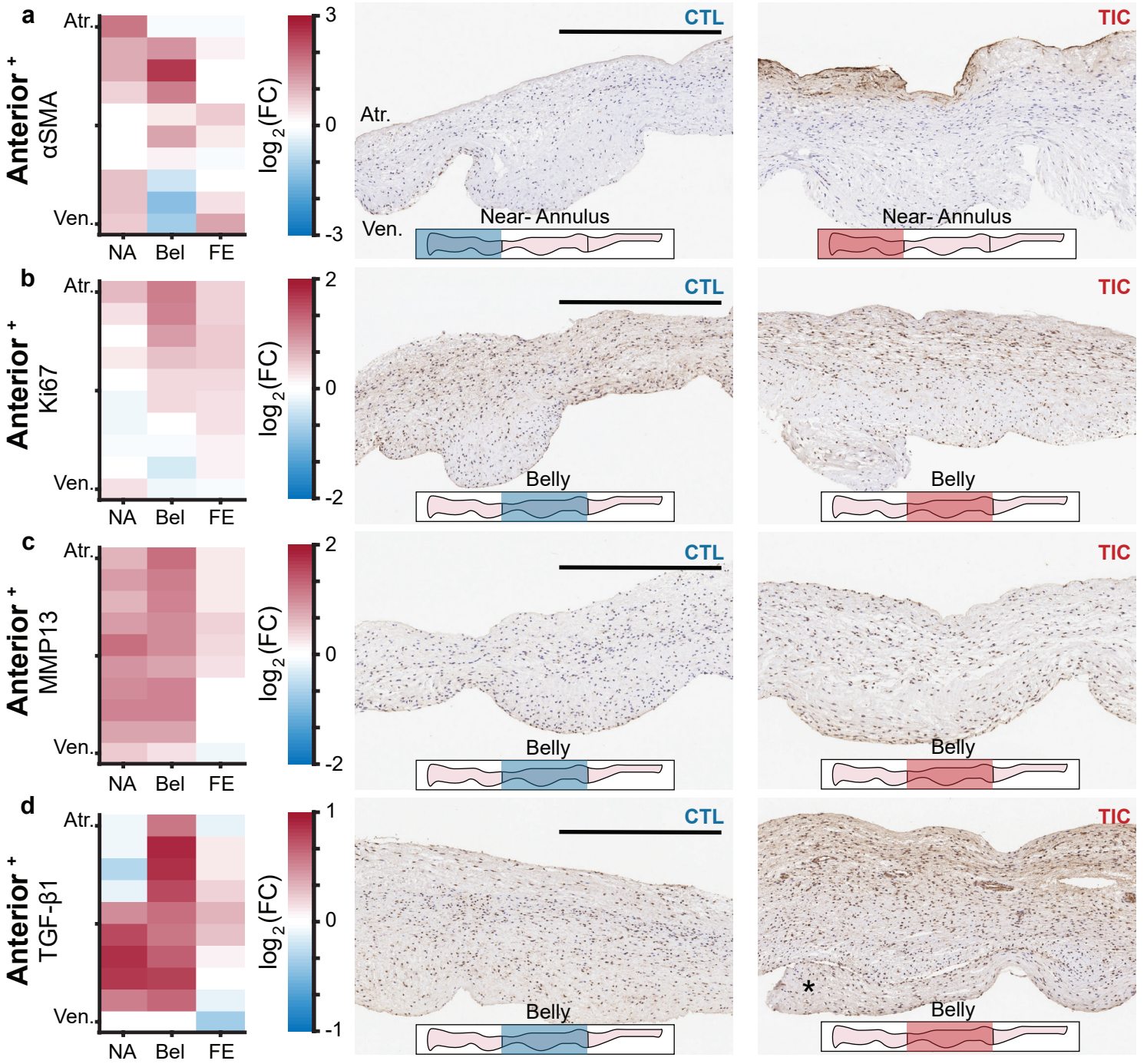
a
Anterior +
αSMA
Atr.
Ven.
NA
Bel
FE
log2(FC)
3
0
-3
CTL
TIC
Atr.
Ven.
Near- Annulus
b
Anterior +
Ki67
2
-2
Belly
c
Anterior +
MMP13
d
Anterior +
TGF-β1
1
-1
*

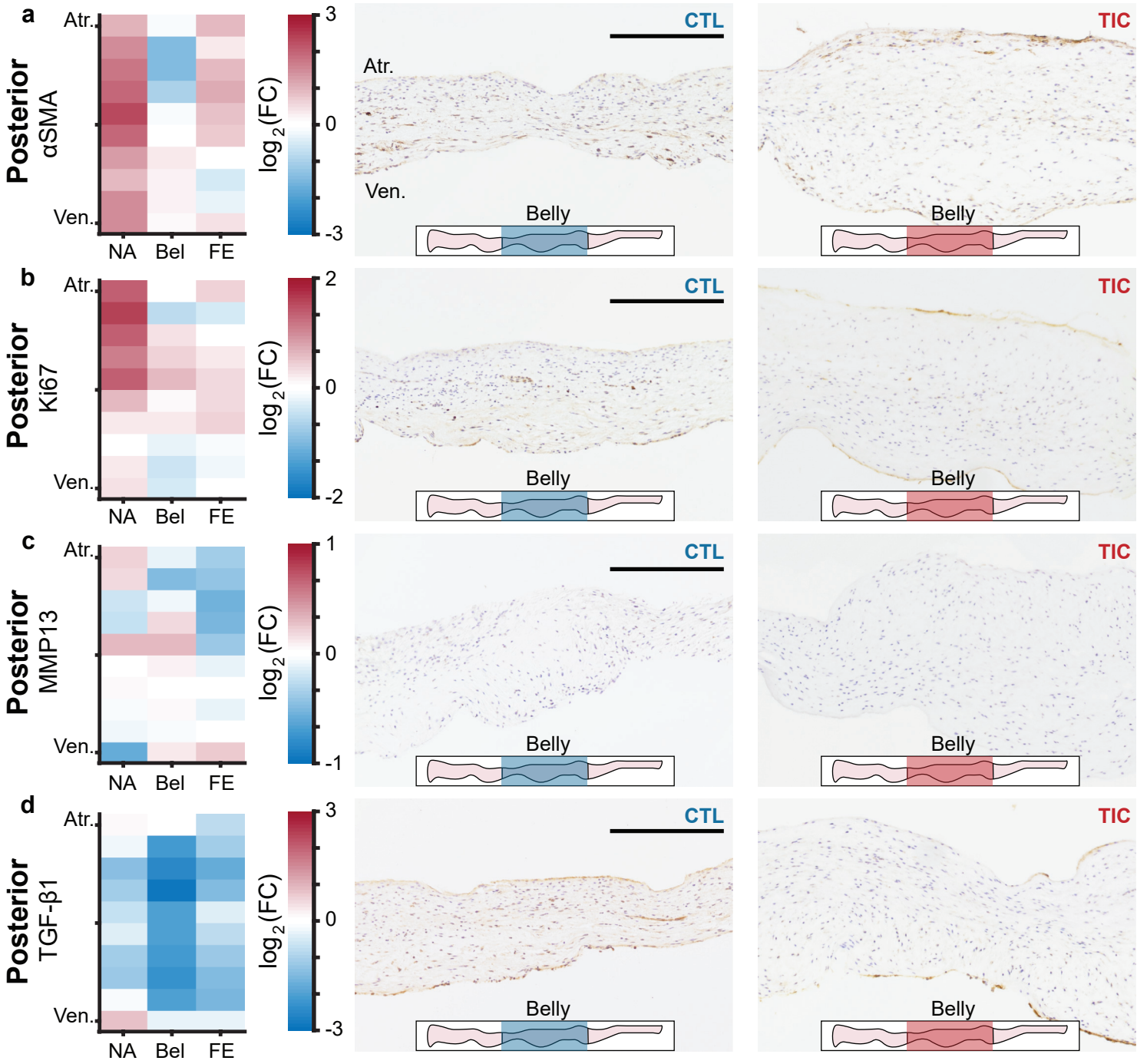
a
Posterior
αSMA
Atr.
Ven.
NA
Bel
FE
log2(FC)
3
0
-3
CTL
TIC
Atr.
Ven.
Belly
b
Posterior
Ki67
2
0
-2
c
Posterior
MMP13
1
0
-1
d
Posterior
TGF-β1
3
0
-3

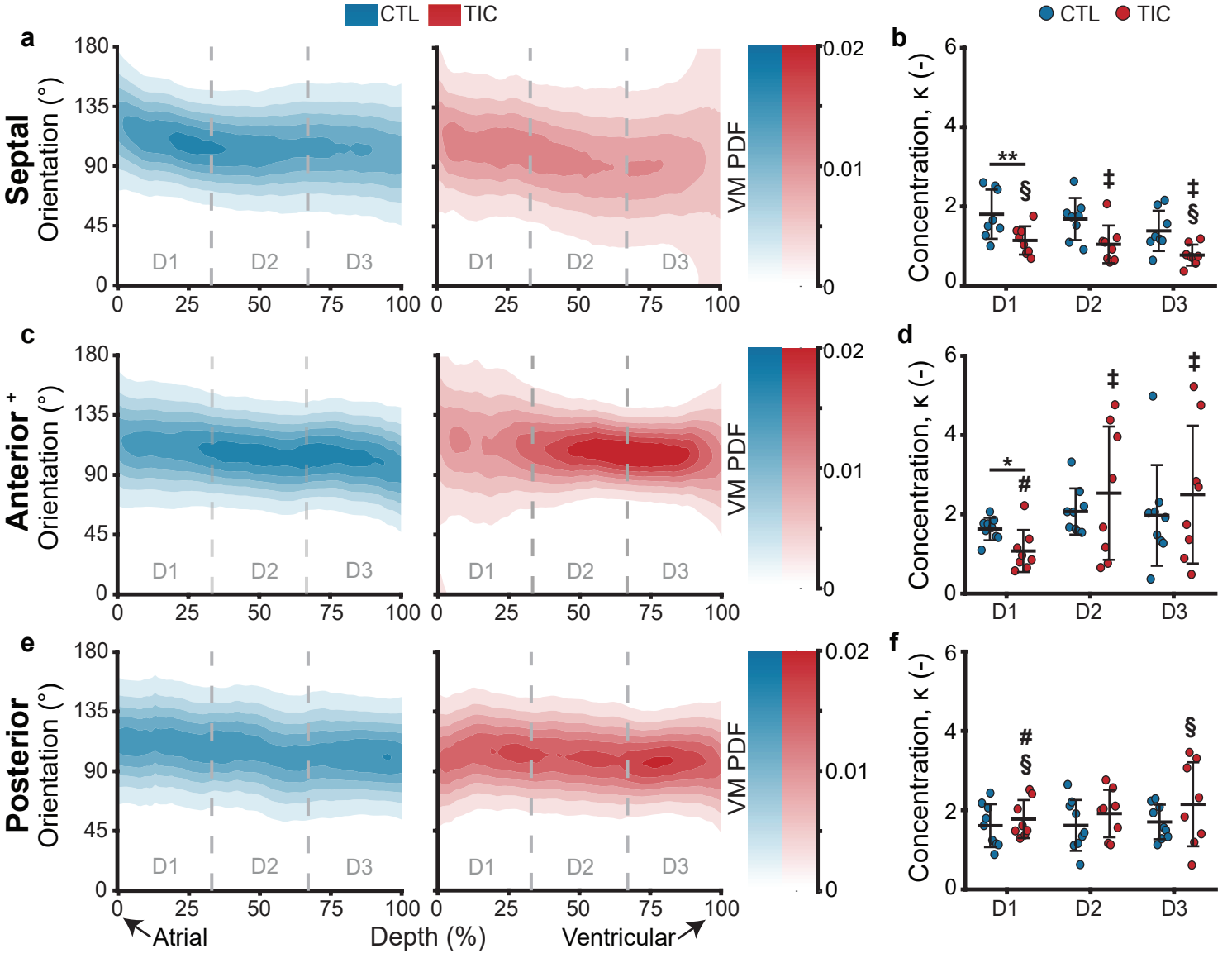
CTL
TIC
a
b
c
d
e
f
Septal
Anterior +
Posterior
Orientation (°)
180
135
90
45
0
D1
D2
D3
0
25
50
75
100
VM PDF
0.02
0.01
0
Concentration, κ (-)
6
4
2
0
**
*
§
‡
#
Atrial
Depth (%)
Ventricular